CHEMISTRY OF MATERIALS

pubs.acs.org/cm Article

Interparticle Antigalvanic Reactions of Atomically Precise Silver Nanoclusters with Plasmonic Gold Nanoparticles: Interfacial Control of Atomic Exchange

Published as part of Chemistry of Materials virtual special issue "C. N. R. Rao at 90".

Paulami Bose, Jayoti Roy, Vikash Khokhar, Biswajit Mondal, Ganapati Natarajan, Sujan Manna, Vivek Yadav, Anupriya Nyayban, Sharma S. R. K. C. Yamijala,* Nonappa,* and Thalappil Pradeep*

Cite This: https://doi.org/10.1021/acs.chemmater.4c00620 Read Online

ACCESS | Metrics & More | Article Recommendations | Supporting Information

ABSTRACT: This work demonstrates that antigalvanic reactions (AGRs) between thiol-protected plasmonic gold nanoparticles (NPs) and atomically precise silver nanoclusters (NCs) are an interfacial chemistry-driven phenomenon. We reacted 2,4-dimethylbenzenethiol (DMBT)-protected Au NPs (average diameter of 4.46 ± 0.64 nm) with atomically precise $[Ag_{25}(DMBT)_{18}]^-$ NC and obtained bimetallic AgAu@DMBT alloy NPs. Systematic investigations with optical absorption spectroscopy, high-resolution transmission/scanning transmission electron microscopy, and elemental mapping revealed the reaction-induced morphological and compositional transformation in NPs. Furthermore, we show that such AGRs get restricted when geometrically rigid interfaces are used. For this, we used 1,3-benzenedithiol (BDT)-protected Au@BDT NPs and $[Ag_{29}(BDT)_{12}(TPP)_4]^{3-}$ NCs (TPP = triphenylphosphine). Electrospray ionization mass spectrometric (ESI MS) studies revealed that the interparticle reaction proceeds via metal−ligand and/or metal exchange, depending on the interface. Density functional theory (DFT) calculations and molecular docking simulations were used to understand the interactions and reaction energetics leading to favorable events. Interfacial chemistry of this kind might offer a one-pot synthetic strategy to create ultrafine bimetallic NP-based hybrid materials with potential optoelectronic and catalytic applications.

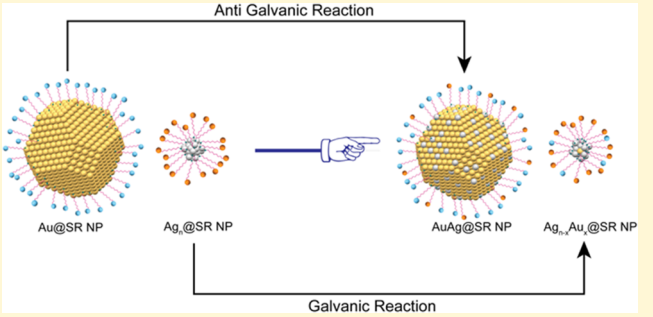

1. INTRODUCTION

Bimetallic nanoparticles (NPs) have attracted significant interest in view of their enhanced catalytic[1,2] and plasmonic performance.[3,4] Common synthetic routes to bimetallic NPs include coreduction, thermal breakdown, seed-mediated growth, and galvanic replacement processes.[5] Classical galvanic reaction (GR), where a noble metal cation is reduced by a less noble ion, is known for its high tunability and efficiency in producing bimetallic NPs.[6−9] However, the antigalvanic reactions (AGRs), namely, the reduction of metal ions by less reactive (or more noble) metals, were considered impossible. Such a reaction was demonstrated using atomically precise nanoclusters (NCs).[10,11] Atomically precise metal NCs are classified as molecular materials in view of their precise composition and well-defined electronic structure, physicochemical, and optical properties.[12−17] The reduction potential of metal NPs decreases as the particle size reduces.[18−20] Specifically, in the context of ultrasmall ligand-stabilized Au NPs, their oxidation potential becomes notably lower than the reduction potential of a few less noble metal ions.[21−23] Choi et al. first identified the $[Au_{24}Ag(SR)_{18}]^-$, $[Au_{24}Ag_2(SR)_{18}]^-$, and other doped species upon mixing $[Au_{25}(SR)_{18}]^-$ NC with Ag-thiolate, using mass spectrometry.[25] Later, Wu reported reactions of neutral $[Au_{25}(SR)_{18}]^0$ and other ultrasmall Au and Ag NPs (sized below 3 nm) with metal ions of Ag and Cu.[26] $[Au_{25}(SR)_{18}]^-$ NC was considered a unique candidate for AGR as Ag^+ ions failed to react with 2−3 nm Au NPs.[27] Wu et al. reported that the oxidation potential of ligand-free Au NPs was lower than the reduction potential of Ag^+, leading to the oxidation of gold NP and reduction of Ag^+, upon mixing the two species.[28] Similarly, Jin et al. demonstrated a similar size dependence on the redox potentials of the 11-mercaptoundecanoic acid (MUA)-protected Au particles.[29] Pattadar et al. reported a size-dependent AGR reactivity of

Received: March 2, 2024
Revised: May 14, 2024
Accepted: May 16, 2024

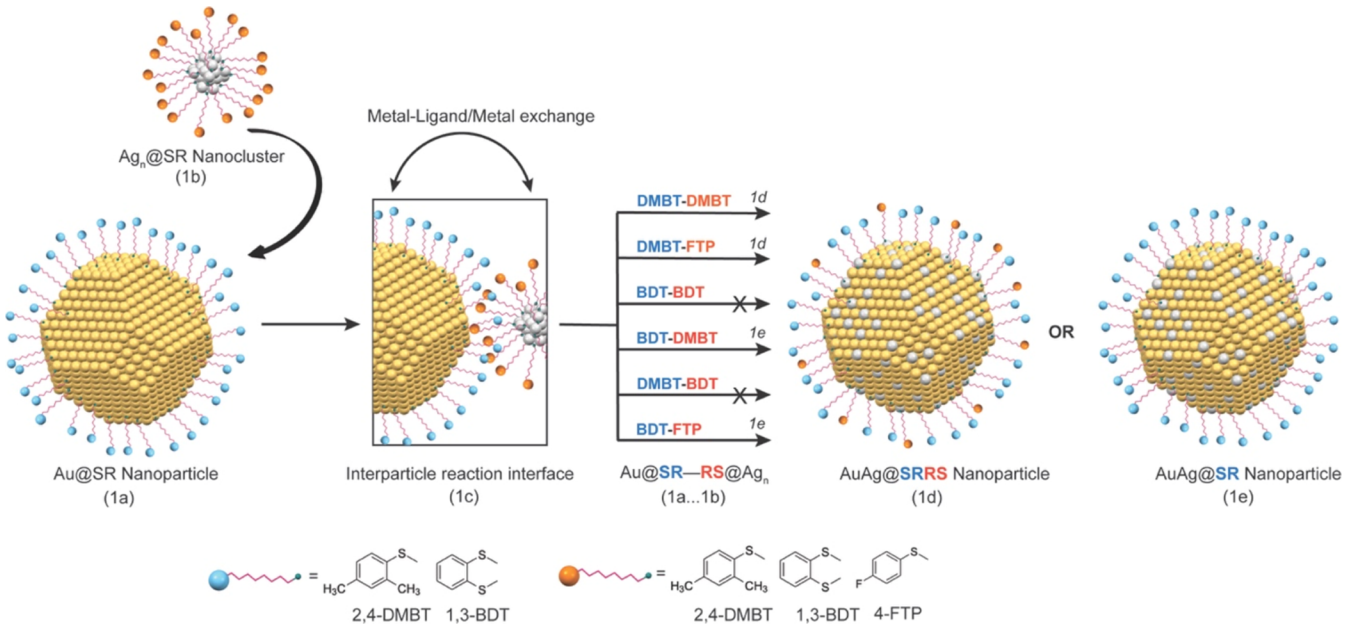

Figure 1. Schematic illustration of the AGRs in Au@SR NP with atomically precise Ag$_n$@SR NCs via intersystem exchange resulting in bimetallic AuAg@SR NPs. SR corresponds to 2,4-DMBT, 1,3-BDT, and 4-FTP; detailed ligand structures are omitted for clarity. Au@DMBT and Au@BDT NPs are denoted by the label Au@SR. Ag$_n$@SR refers to $[Ag_{25}(DMBT)_{18}]^-$, $[Ag_{44}(FTP)_{30}]^{4-}$, $[Ag_{44}(FTP)_{30}]^{3-}$, and $[Ag_{29}(BDT)_{12}(TPP)_4]^{3-}$ NCs. As indicated, Au@BDT−Ag$_n$@BDT and Au@DMBT−Ag$_n$@BDT reactions do not occur. Color code: yellow, Au; gray, Ag; green, S; pink-blue/orange, ligand. Note that the atomic dimensions and particle sizes are significantly underestimated to suit the representation.

weakly stabilized and surface-attached Au NPs (diameter ranging between 1 and 4 nm) with Ag^+ or $PtCl_4^{2-}$ ions.[23] The ligand monolayer on the NC surface plays a prominent role in AGRs.[16,22−24] Sahu and Prasad reported the solution phase reaction involving Au@DDA (DDA = dodecylamine) and Au@DDT (DDT = dodecanethiol) NPs with Ag^+ ions, yielding Au@Ag core−shell and monometallic Ag and Au NPs, respectively, at 90 °C.[30] The architecture of the resulting NPs was found to be influenced by the nature of ligand binding to the metal NP surface, with excess DDA and DDT ligands facilitating the reduction of Ag^+ to Ag^0. Studies also revealed that the heteroatom addition or replacement resulted in alloyed Au NC with either the retention[31] or an alteration of its original structural framework.[32] Ligands facilitate the formation of heterometallic NC frameworks.[33−35] However, most reports on AGRs are limited to atomically precise ultrasmall NPs with sizes smaller than 3 nm.[10] Considering AGRs from the perspective of interfacial chemistry may help address such processes with plasmonic NPs.[36]

Atomic exchange during nanocluster−nanoparticle (or interparticle) reactions is a relatively less explored area of study. Ligand-exchange,[37−45] metal-exchange,[46−49] and isotopic-exchange[50−52] reactions of atomically precise metal NCs are well-known.[13,14,36,53,54] Like molecules, atomically precise metal NCs undergo internanocluster (or intercluster) reactions in solution.[55−57] Bimetallic and trimetallic NCs have also been prepared using intercluster reactions.[15,58] Studies on the intercluster reaction mechanism suggest a pathway for the exchange of metal or metal−ligand fragments.[55] The thiolate monolayer protecting the NC surface is dynamic in nature,[59,60] and the metal−ligand interface controls the atom transfer in an intercluster reaction.[61] However, most examples of interparticle interactions are purely driven by supramolecular interactions, such as hydrogen-bonding, van der Waals, C−H···π, π···π, and electrostatic interactions where the reacting particles retain their intrinsic properties in the superstructures.[54,62−70] We recently reported the formation of a self-assembled 2D superlattice of monodispersed Ag−Au−alloy NPs by reacting polydispersed Ag NPs with $[Au_{25}(SR)_{18}]^-$ NC.[71] As studied using mass spectrometry, the reaction mechanism suggested an interparticle atomic exchange (metal−ligand species), and the metal−ligand interface was crucial for the reaction.[59] Kazan et al. showed that the thiol acts as a messenger in the metal−atom exchange between the NC and the surface in such reactions.[72] A later study on the kinetics of isotopic exchanges showed a size dependence when the reacting partner was varied from the nanoscale to bulk metal with an isotopically pure $[Ag_{25}(SR)_{18}]^-$ NC.[52] A recent study showed $[Ag_{25}(SR)_{18}]^-$ NC-meditated site-selective etching of anisotropic Au nanotriangles (Au NTs).[73] Roy et al. reported $[Au_{25}(SR)_{18}]^-$ and CuO NP reaction, which induced the aggregation of Cu-doped NC leading to spherical superstructures.[74] The feasibility of interparticle reactions and the dynamics at the metal−ligand interface across the gold−silver system of all dimensions is a natural extension of this problem.

Self-assembled colloidal NP-based, also known as supraparticles, hybrid materials are known for their potential catalytic,[75] optoelectronic,[76,77] and biological applications.[78] In reference to our previous and current studies, we presume that modulating the reaction microenvironment (temperature and solvent, for instance) and/or the protecting ligand of NPs could potentially facilitate their assembly into supraparticles, such as superlattices,[71] nanodiscs,[74] and nanodumbbells.[62] For example, nanodiscs may find potential applications as nanoflasks for catalysis[79,80] and selective ion capture.[81] NP superlattices may find prominence in optoelectronic applications, for example, surface-enhanced Raman scattering (SERS)-based sensors,[82] nanoscale devices,[83] and many more possibilities.[84] In the future, we intend to utilize our concept of

https://doi.org/10.1021/acs.chemmater.4c00620
Chem. Mater. XXXX, XXX, XXX−XXX

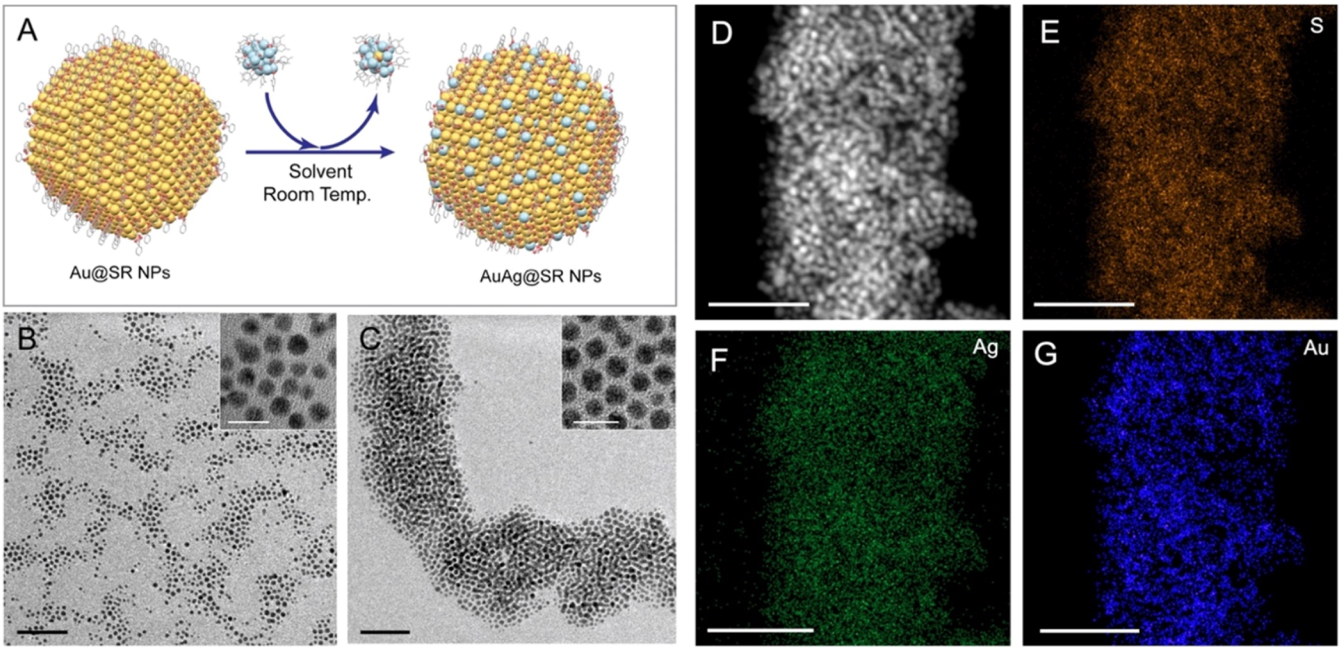

Figure 2. Schematic representation of the interparticle reaction between Au@SR NP and $[Ag_{25}(SR)_{18}]^-$ NC, where SR = 2,4-DMBT (A). TEM images of Au@DMBT NPs before (B) and after (C) the reaction. Dark-field STEM image of the reacted NPs (D) and the corresponding EDS maps of S (E), Ag (F), and Au (G). Scale bars: 50 (B–G) and 10 nm (insets of B and C). Color code in A: yellow, Au; blue, Ag; pink, S; gray, C. H has been omitted for clarity. Note that the ligand structure and anchoring sites are not a true representation of the NP.

interparticle chemistry to develop ultrafine bimetallic NP-based hybrid nanomaterials for such promising optoelectronic and catalytic applications.

Herein, we report the phenomenon of AGR in plasmonic Au NPs by performing interparticle reaction between Au@SR NPs and atomically precise Ag@SR NCs (schematically illustrated in Figure 1). To demonstrate the effect of the metal–ligand (SR-Au···Ag-SR) interface, NPs and NCs protected with monodentate and bidentate thiols, as well as mixed monolayers, were investigated. This work establishes that interparticle reactions are universal across noble metal systems. With the right choice of a particle system, we can now create bimetallic NPs and size-focus them all in one pot, simultaneously. This leads us to propose that atom transfer between NP and NC during interparticle reactions is a potential pathway to AGRs.

2. EXPERIMENTAL SECTION

The materials and methods for the syntheses of NPs, Au@DMBT, and Au@BDT, and the NCs, $[Ag_{25}(DMBT)_{18}]^-$, $[Ag_{29}(BDT)_{12}(TPP)_4]^{3-}$, and $[PPh_4]_n[Ag_{44}(FTP)_{30}]$ (where, n = 3, 4) are included in the Supporting Information (SI 1). Here, the protecting ligands on the particles, such as DMBT, BDT, FTP, and TPP, correspond to 2,4-dimethylbenzenethiol, 1,3-benzenedithiol, 4-fluorothiophenol, and triphenylphosphine, respectively.

2.1. Interparticle Reactions. Initially, a stock solution of NCs (1.0 mg/10 mL) was prepared in the relevant solvent based on its highest solubility. $[Ag_{25}(DMBT)_{18}]^-$ and $[PPh_4]_n[Ag_{44}(FTP)_{30}]$ (where, n = 3, 4) NCs were dissolved in DCM. $[Ag_{29}(BDT)_{12}(TPP)_4]^{3-}$ NC was dissolved in DMF. Then, a solution of Au@DMBT and Au@BDT NPs (5.0 mg/3 mL) was prepared in DCM and DMF, respectively. 0.3 mL of NC was added to the NP solution and allowed to react under rest. The reaction was monitored using high-resolution transmission electron microscopy (HRTEM) and optical absorption spectroscopy. The detailed concentration calculations are presented in the SI. In the subsequent text, this experiment is referred to as reaction@NP.

2.2. Mass Spectral Measurements. We performed electrospray ionization mass spectrometry (ESI MS) using Waters Synapt G2-Si instrument. From the stock solutions, 1 mL of NC and 0.3 mL of NP were mixed, and the reaction mixture was diluted with solvent (DCM or DMF, depending on the particle solubility) while maintaining the total volume at 6 mL. Then, the required volume was taken for time-dependent ESI mass and optical absorption spectral studies. The concentration calculations are presented in the SI. In the subsequent text, these ESI MS measurements are referred to as reaction@NC.

In simple terms, the interparticle reaction (referred to as reaction@NP) requires an excess of Au NPs (for example, 2.50 μM Au@DMBT NP reacts with 1.75 μM $[Ag_{25}(DMBT)_{18}]^-$ NC), while the mass spectral study (referred to as reaction@NC) necessitates an excess of Ag NC (3.22 μM Au@DMBT NP reacts with 0.12 μM $[Ag_{25}(DMBT)_{18}]^-$ NC) to thoroughly comprehend the reaction mechanism (detailed concentration calculations are provided in the Supporting Information, SI 2).

3. RESULTS AND DISCUSSION

3.1. Interparticle Reaction at Structurally and Compositionally Analogous Metal-Monodentate Ligand Interface. Interparticle reaction between a plasmonic Au@DMBT NP and atomically precise $[Ag_{25}(DMBT)_{18}]^-$ NC and the consequent reaction pathway leading to the final product is schematically illustrated in Figure 2A (see the SI for additional data and complete characterization). We prepared Au@DMBT NPs with an average diameter of 4.46 ± 0.64 nm using a modified Brust–Schiffrin method (synthetic procedures in the SI 1). Hereafter, the 2,4-DMBT-capped-Au NPs are referred to as ∼4.5 nm Au@DMBT NPs. TEM image of the parent Au@DMBT NPs is presented in Figure 2B (further details in the SI, Figure S1). The optical absorption spectrum of Au@DMBT NP has a characteristic localized surface plasmon resonance (LSPR) peak at 520 nm (Figure S1). We utilized the $[Ag_{25}(DMBT)_{18}]^-$ NC synthesized using a reported protocol.[85] The mass spectrum and optical absorption spectral data of the pure Ag NC are provided in Figure S2. In

https://doi.org/10.1021/acs.chemmater.4c00620
Chem. Mater. XXXX, XXX, XXX–XXX

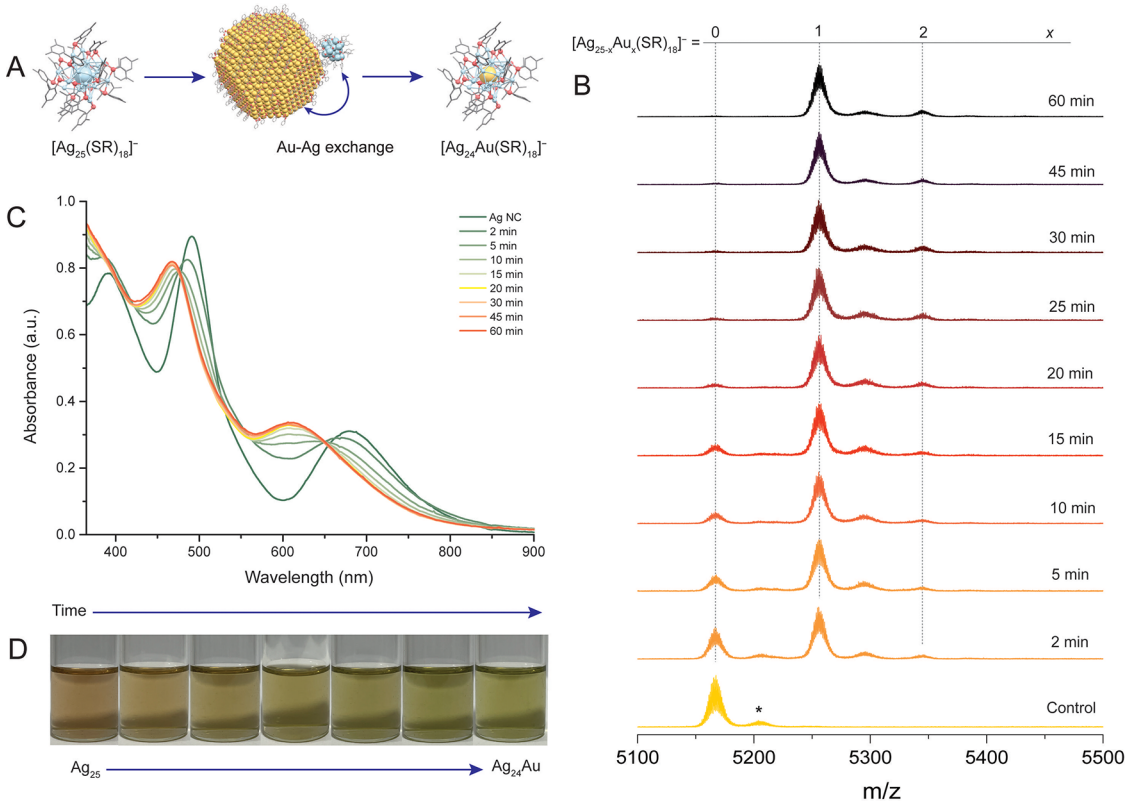

Figure 3. (A) Schematic representation of the metal-exchange pathway as the NC interacts with NP. (B) Time-dependent ESI mass spectra of the interparticle reaction. (C) Corresponding optical absorption spectra of the reaction and (D) resulting change in the color of the solution. The peak labeled * in panel B is due to unidentified contamination. Color code in panel A: yellow, Au; blue, Ag; pink, S; gray, C. H has been omitted for clarity.

the negative ion ESI MS, the $[Ag_{25}(DMBT)_{18}]^-$ NC showed a molecular ion peak centered at m/z 5166, with unidentified contamination at m/z 5204 (refer to the control sample of Figure 3B and full range spectrum in Figure S2A). For our experiment, we mixed known volumes of Au@DMBT NP (2.5 μM) and $[Ag_{25}(DMBT)_{18}]^-$ NC (1.75 μM) solutions in DCM at room temperature (refer to the Experimental Section and SI for a description of the calculations of concentrations, SI2). TEM of the reacted Au NPs is presented in Figure 2C (additional data in Figure S3). We estimated the particle size distribution from the most probable diameter of the metallic core of multiple NPs as observed in TEM. The average size of Au@DMBT NPs changes from 4.46 ± 0.64 nm (d-spacing 0.28 nm, fwhm 1.51 nm) to 4.81 ± 0.59 nm (d-spacing 0.27 nm, fwhm 1.40 nm) before and after the reaction, respectively (Figure S4). A slight shift in the distribution toward a lower fwhm value for the reacted Au NPs suggests an onset of size-focusing compared to the parent Au NP.

The effect of alloying on surface plasmon resonance (SPR) in Au and Ag NPs has been studied widely.[86] Insertion of Ag-atoms into a Au NP strongly alters the plasmon resonance and leads to a shift in the peak position depending upon the structure and composition of the alloy NP.[87,88] The optical spectra of the reaction mixture showed a continuous evolution, indicating spontaneous solution phase dynamics (Figure S5). The system took 30 min to reach equilibrium after particle mixing; visible spectral changes appeared as early as 2 min. Upon reaction with $[Ag_{25}(SR)_{18}]^-$ NC, the reaction mixture exhibited a blue shift of ∼31 nm in the SPR compared to the parent Au NP, resulting in a modified peak at 488 nm. Such a change in the spectral feature indicates the insertion of Ag-atoms in the parent Au NP. The scanning transmission electron microscopy−energy-dispersive X-ray spectroscopy (STEM−EDS)-based elemental maps of gold (Au M), silver (Ag L), and sulfur (S K) of the reacted NPs are presented in Figure 2D−G. Elemental mapping images of Au−Ag−S showed a uniform distribution across particles, indicating the formation of well-alloyed bimetallic Au−Ag-thiolated hybrid NPs. The EDS spectra collected from various locations on the grid loaded with the reacted NP sample showed a higher Au content compared to Ag (Figure S6).

Our previous work utilized ESI MS to study interparticle reaction mechanisms.[52,71] Mass spectrometry can track the chemical changes occurring in a Au NC as it reacts with the Au NP, providing mechanistic insight into such reactions. We performed a time-dependent ESI MS of the particle mixture with constant mass spectrometric parameters (refer to the Experimental Section). Such interparticle systems are referred to as reaction@NC in the subsequent text. Figure 3A schematically illustrates that the Au@DMBT NP and $[Ag_{25}(DMBT)_{18}]^-$ NC reactions proceed via a spontaneous intersystem metal-exchange pathway (details on the ratio of particle mixing are in the SI). NP−NC reactions are spontaneous and stoichiometric in nature.[52,71] Figure 3B shows the time-dependent evolution of the mass spectral features of $[Ag_{25}(DMBT)_{18}]^-$ NC upon interaction with Au NP (full range MS in Figure S7). As the reaction progressed, the peak corresponding to the parent species, $[Ag_{25}(DMBT)_{18}]^-$ NC (m/z 5166), gradually shifted toward a higher mass species, $[Ag_{24}Au(DMBT)_{18}]^-$ NC (m/z 5255),

https://doi.org/10.1021/acs.chemmater.4c00620
Chem. Mater. XXXX, XXX, XXX−XXX

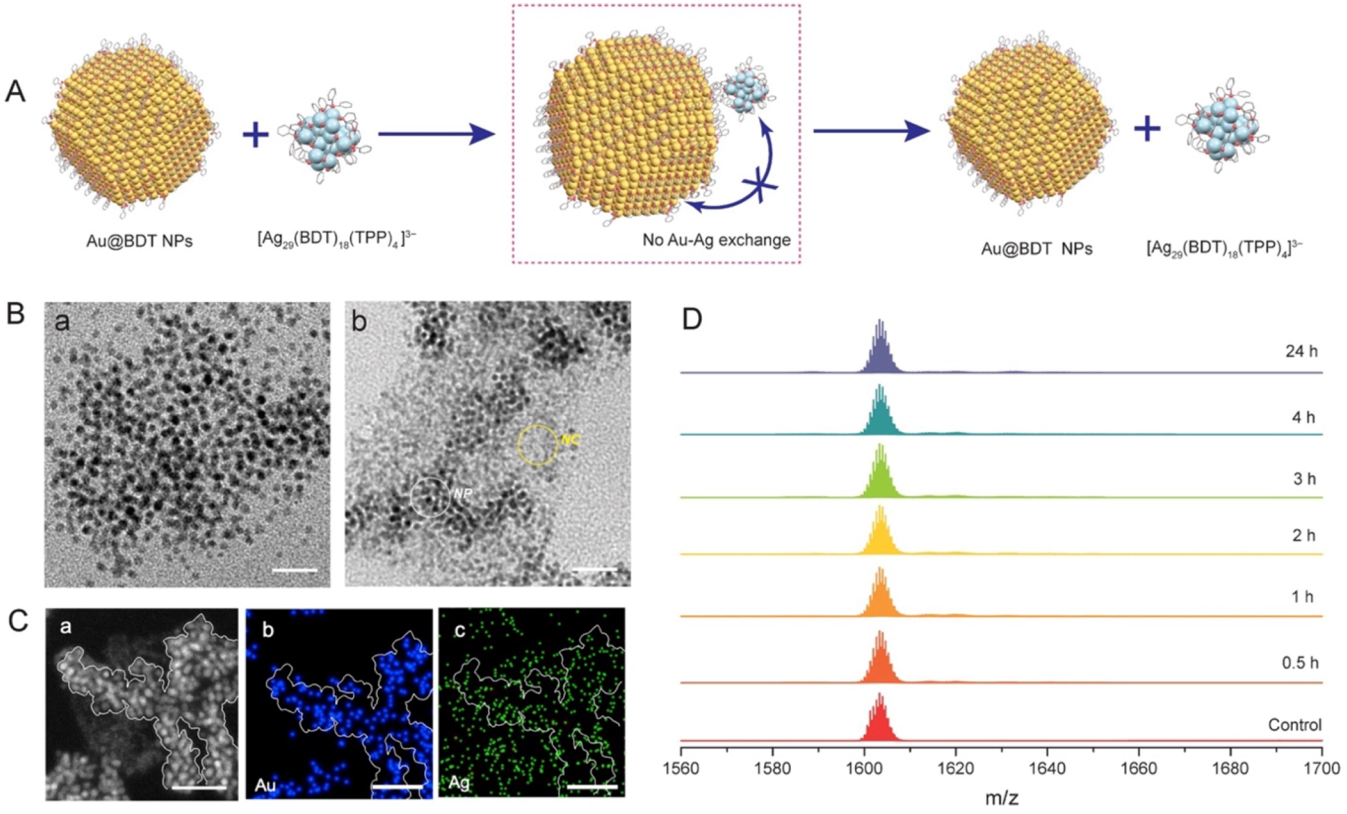

Figure 4. (A) Schematic illustration of a nonreactive 1,3-BDT-protected Au NP and Ag NC interactions. (B) TEM images of the parent Au@BDT NPs (a) and unreacted Au@BDT NPs/$[Ag_{29}(BDT)_{12}(TPP)_4]^{3-}$ NC in the reaction mixture (b). (C) Dark-field STEM image of the reaction mixture (a) and the corresponding EDS maps showing the footprint of elemental Au (b) and Ag (c). (D) Time-dependent ESI mass spectra of the reaction@NC. Scale bar: 20 nm. Color code: yellow, Au; blue, Ag; pink, S; gray, C; H is omitted.

and complete conversion of the former occurred within 30 min. The mass difference with the newly emerged peaks is ~89 Da, which corresponds to a simultaneous Ag (108 Da) loss and Au (197 Da) addition into the $[Ag_{25}(DMBT)_{18}]^-$ NC. In addition to the first-doped NC species, $[Ag_{23}Au_2(DMBT)_{18}]^-$ NC (m/z 5344) was also observed at a reasonable intensity (isotopic distribution patterns in Figure S8). Similarly, the prominent optical absorption spectral features of $[Ag_{25}(DMBT)_{18}]^-$ NC showed a gradual and continuous blue shift as the reaction progressed (Figure 3C). Within 30 min of reaction, the spectral features of the parent NCs evolved into two major features at 470 and 610 nm, resembling the previously reported $[Ag_{24}Au(DMBT)_{18}]^-$ NC.[89] The $[Ag_{25}(DMBT)_{18}]^-$ NC reaction with Au@DMBT NP causes a gradual change in the color of the reaction mixture from brown to olive-green with time (Figure 3D). The reacted NC exhibited an ~ 6.8-fold enhancement in photoluminescence compared to the parent $[Ag_{25}(DMBT)_{18}]^-$ NC; a similar phenomenon was reported by Bootharaju et al. (Figure S9).[89]

In this section, we correlated the results of the reaction@NP and reaction@NC to propose an overall reaction mechanism for the interparticle reaction between Au NP and Ag NC. Previous ESI MS observations confirm that the NC-NP reaction takes place along a pathway involving atomic exchange between particles. The MS studies of the reacted Au NP indicated that the parent $[Ag_{25}(DMBT)_{18}]^-$ NC undergoes complete consumption during the reaction (Figure S10). From the absence of luminescence in the reacted Au NP solution, as seen in the photoluminescence spectra and photographed under UV light, it can be further inferred that the alloying process via interparticle reaction involves the complete consumption of both the parent $[Ag_{25}(DMBT)_{18}]^-$ NC and the intermediate $[Ag_{25-x}Au_x(DMBT)_{18}]^-$ NC species (Figure S9). Figure S11 presents TEM images comparing the particle morphologies of the reactants and the products. Therefore, it can be presumed that the smaller NC, upon interaction with the NP, undergoes intersystem atom transfer and eventually gets completely consumed by the larger NPs, resulting in the formation of alloy NPs.

3.2. Interparticle Reaction at Structurally and Compositionally Analogous Metal-Bidentate Ligand Interface. We studied the interparticle reaction by modifying the particle monolayer with a bidentate-capping ligand called 1,3-benzenedithiol (BDT). It is already known that the dithiol-protected NCs show distinctly different chemistry at the metal−ligand interface compared to the monothiolated ones.[90] Ghosh et al. showed that in the intercluster reactions, dynamics at the metal−ligand interface could be altered with the dithiolates binding to the metal core in a bidentate manner, which, in turn, reduces the flexibility of the interface.[91]

The overall reaction for a dithiol-capped particle system, 1,3-BDT-protected plasmonic Au NPs (to be referred to as Au@BDT NPs) and atomically precise $[Ag_{29}(BDT)_{12}(TPP)_4]^{3-}$ NC, is schematically represented in Figure 4A (see the SI for experimental and characterization data). We synthesized the Au@BDT NPs with an average size of 3.70 ± 0.48 nm using a modified Brust−Schiffrin method (TEM image in Figure 4B-a, and further characterization in Figure S12).[92] The ESI MS of the pure $[Ag_{29}(BDT)_{12}(TPP)_4]^{3-}$ NC shows a molecular ion peak centered at m/z 1603 after the loss of 4 TPP ligands

https://doi.org/10.1021/acs.chemmater.4c00620
Chem. Mater. XXXX, XXX, XXX−XXX

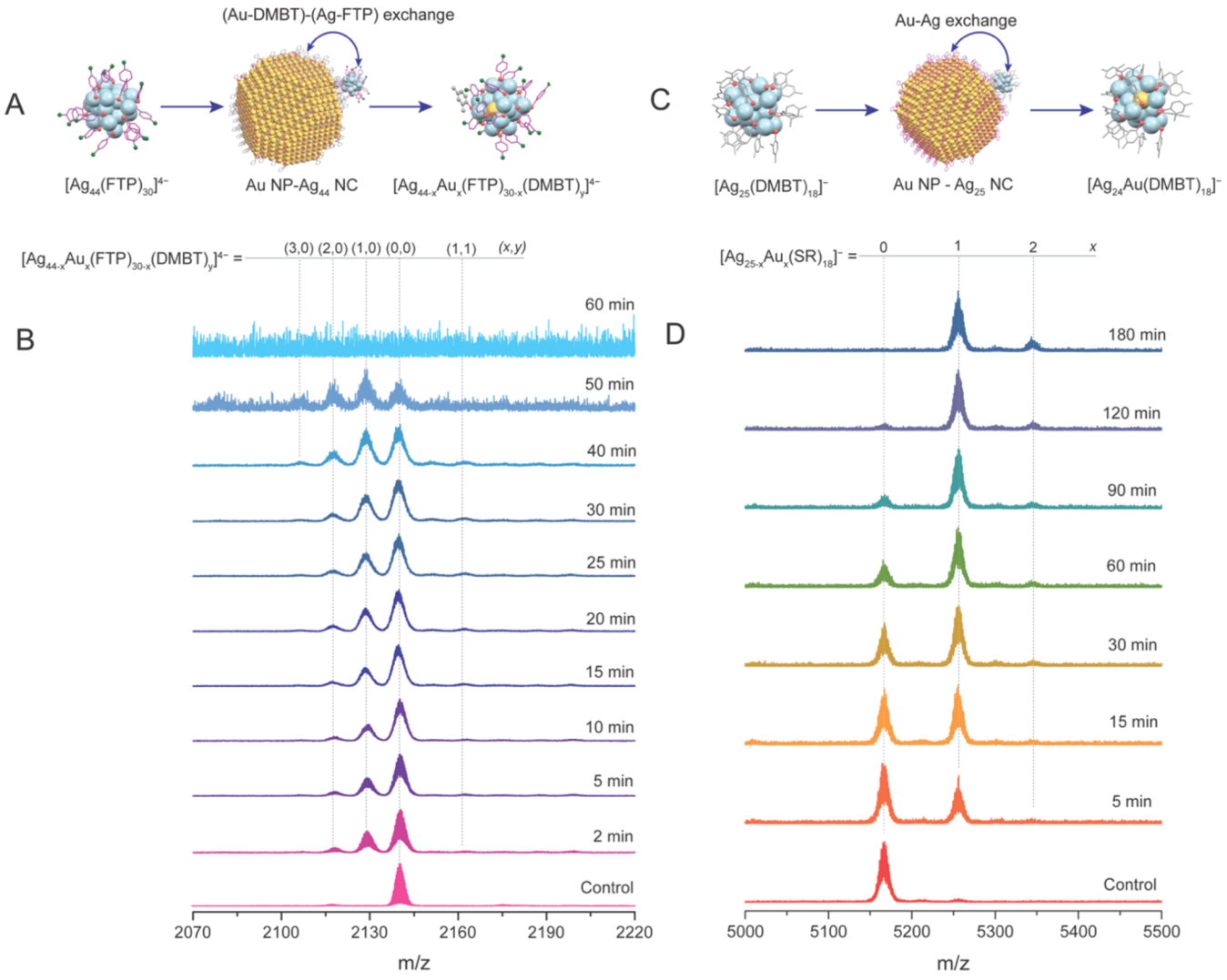

Figure 5. Schematic representation of the interparticle reaction between (A) Au@DMBT NP and $[Ag_{44}(FTP)_{30}]^{4-}$ NC and (B) corresponding time-dependent ESI mass spectra for the reaction@NC. (C) Au@BDT NP and $[Ag_{25}(DMBT)_{18}]^{-}$ NC reaction and (D) corresponding time-dependent ESI mass spectra. Color code: yellow, Au; blue, Ag; pink, S; magenta/gray, C; green, F; H was omitted for clarity.

during electrospray ionization (characterization details in Figure S13).[93] For the study of reaction@NP, we mixed known volumes of Au@BDT NP (4.6 μM) and $[Ag_{29}(BDT)_{12}(TPP)_4]^{3-}$ NC (1.55 μM) solutions in DMF at room temperature (refer to the Experimental Section and concentration calculation in the SI). In Figure 4B-b, the TEM image of the reaction@NP mixture shows an unreacted particle mixture, where the particles with higher and lower contrasts correspond to Au@BDT NPs (highlighted in white) and subnanometer $[Ag_{29}(BDT)_{12}(TPP)_4]^{3-}$ NCs (highlighted in yellow), respectively. The optical absorption spectra of the constituent particles in the mixture were stable after 24 h of mixing, further confirming that there were no interparticle interactions (Figure S14). A comparative TEM image of the starting materials and the reaction mixture imaged after 30 min and 24 h of mixing are provided in Figure S15. In Figure 4C, the STEM−EDS-based elemental maps show the Au M (Figure 4C-b), and Ag L (Figure 4C-c) translocation across the interparticle reaction mixture (note that the white outline indicates the NP-rich region). The Au M mapping (Figure 4C-b) appears weak in the regions where Au NPs are lesser in concentration. In contrast, the Au-deficit regions showed higher Ag intensity in the Ag L mapping (Figure 4C-c). Therefore, elemental mapping also indicates that the analyte is composed of unreacted Au and Ag particles. Quantitative STEM−EDS spectra of the Au NP before and after mixing with $[Ag_{29}(BDT)_{12}(TPP)_4]^{3-}$ NC are provided in Figure S16.

We performed the ESI MS experiment to further confirm that the interparticle mixture does not include an atomic exchange between the systems. For the reaction@NC study, we mixed known volumes of Au@BDT NP (0.23 μM) and $[Ag_{29}(BDT)_{12}(TPP)_4]^{3-}$ NC (2.85 μM) solutions in DMF at room temperature and analyzed the reaction mixture (refer to the Experimental Section and concentration calculation in the SI). All of the mass spectrometric parameters were kept constant during the entire measurement. The MS peak corresponding to $[Ag_{29}(BDT)_{12}]^{3-}$ NC (m/z 1603) remained intact in the reaction mixture even after 24 h. The corresponding optical spectral data given in Figure S17 agrees with the mass spectral observations. Therefore, we conclude that Au@BDT NP and $[Ag_{29}(BDT)_{12}(TPP)_4]^{3-}$ NC are nonreactive, allowing the parent particles to retain their inherent chemical properties. From the above study, we infer

https://doi.org/10.1021/acs.chemmater.4c00620
Chem. Mater. XXXX, XXX, XXX−XXX

that the introduction of bidentate ligand stabilization into the particle system ultimately inhibits interparticle reactions.

3.3. Role of the Metal−Ligand Interface in an Interparticle Reaction. From the previous discussions, we understand that the monolayers and their nature of bonding to the NP surface are key in controlling their reactivity toward NC.[71] Krishnadas et al. reported the involvement of the metal−ligand (Au-PET−Ag-FTP) fragments in an intercluster reaction between $[Au_{25}(PET)_{18}]^-$ and $[Ag_{44}(FTP)_{30}]^{3-}$.[55] To further investigate the contribution of the ligand in these interparticle (Au NP−Ag NC) events, we have introduced an FTP-protected Ag NC system.

We chose Au@DMBT NP and $[PPh_4]_n[Ag_{44}(FTP)_{30}]$ (where, n = 3, 4) NC as our particle system where Au-DMBT···Ag-FTP acts as a reacting interface (details in the Experimental Section). ESI MS and optical absorption spectral data of the $[PPh_4]_n[Ag_{44}(FTP)_{30}]$ NC are presented in Figure S18. Using similar experimental conditions as for the DMBT-capped particle system, we conducted both reaction@NP and reaction@NC on the Au@DMBT NP—$[PPh_4]_n[Ag_{44}(FTP)_{30}]$ NC system (refer to the Experimental Section). The SI includes microscopic and spectroscopic results for the reaction@NP. As the reaction progressed, the spectral feature corresponding to Au@DMBT NP evolved into an enhanced and blue-shifted SPR at 523 nm in the optical absorption spectra, suggesting a Ag NC-induced chemical change in the parent Au NP (Figure S19). However, the reaction of Au NP with the $[PPh_4]_n[Ag_{44}(FTP)_{30}]$ NC causes a slight increase in their average size, from 4.46 ± 0.64 to 4.72 ± 0.91 nm (Figure S20). The fwhm values are 1.51 and 1.91 nm, calculated from the size distribution of NPs before and after the reaction, respectively.

Figure 5A depicts a schematic representation of the mechanistic pathway for the reaction between Au@DMBT NP and $[Ag_{44}(FTP)_{30}]^{4-}$ NC. As the interparticle reaction progressed, the molecular peak corresponding to the parent species, $[Ag_{44}(FTP)_{30}]^{4-}$ NC (m/z 2140), shifted gradually toward the species with lower m/z values (Figure 5B). The $[Ag_{43}Au(FTP)_{29}]^{4-}$ NC (m/z 2130) was detected as a major species within 2 min in the reaction. The mass difference with the newly emerged peaks is ∼10 Da, which corresponds to a Ag−FTP unit (235 Da) loss from the $[Ag_{44}(FTP)_{30}]^{4-}$ NC and a simultaneous Au (197 Da) addition into it. Along with the first-doped species, $[Ag_{42}Au_2(FTP)_{28}]^{4-}$ (m/z 2120) and $[Ag_{41}Au_3(FTP)_{27}]^{4-}$ (m/z 2111) NC species were detected in a reasonable intensity. The $[Ag_{43}Au(DMBT)(FTP)_{29}]^{4-}$ NC species, as observed at m/z 2164, corresponds to a simultaneous (Ag-FTP)···(Au-DMBT) exchange in the $[Ag_{44}(FTP)_{30}]^{4-}$ NC (isotopic distributions match in Figure S21). Noticeable deviations from the parent $[Ag_{44}(FTP)_{30}]^{4-}$ NC features were observed in the optical spectrum acquired within 2 min of mixing the particles (Figure S22). Most of the spectral features evolved within 30 min into the reaction, and two major features appeared around 412 and 529 nm, with weaker features around 483 and 643 nm. Moreover, we note that such a blue-shifted spectrum resembles the previously reported Au-doped-Ag_{44}@FTP NC.[94,95] We carried out the Raman spectral measurements on the reacted Au NP to confirm FTP-DMBT ligand exchange on the NP surface (refer to the SI for details). As shown in Figure S23, the reacted NP shows distinguishable SERS corresponding to C−X stretching (191−282 cm^{-1}) and deformation (775−877 cm^{-1}), ring breathing (980−1047 cm^{-1}), and C−C stretching (1512−1681 cm^{-1}) frequencies (wavenumber ranges correspond to the AgAu@DMBT, FTP NP), which are characteristic for halogenated thiophenols.[96−98] The presence of an electronegative F atom in the 4-FTP ligand is likely to cause a greater metal−ligand backdonation, leading to a shift in the frequency and relative intensity.[96] From the foregoing results, we infer that the Ag NC-mediated AGR of Au NPs proceeds via a metal−ligand fragment exchange.

3.4. Interparticle Reaction at a Structurally Complex Metal−Ligand Interface. Next, we studied the Au NP−Ag NC reaction at a geometrically complicated interparticle interface, which included dithiolated and monothiolated NPs to provide a range of geometric/structural rigidity and flexibility, respectively. We chose Au@BDT NP and $[Ag_{25}(DMBT)_{18}]^-$ NC as our particle system of interest, where Au-BDT···Ag-DMBT acts as a reacting interface (synthesis and characterization in the SI). Intercluster reactions with BDT-protected metal NCs have been studied extensively in the past. Such reactions usually involve a metal-exchange reaction pathway instead of a metal−ligand exchange.[91] We carried out the reaction@NP and the reaction@NC for the above particle system while keeping the experimental conditions the same as the previous experiments.

The Au@BDT NP and $[Ag_{25}(DMBT)_{18}]^-$ NC reactions involve an intersystem atom exchange, as schematically represented in Figure 5C. In ESI MS measurement as shown in Figure 5D, we observed a steady shift with time in the molecular peak corresponding to the parent species, $[Ag_{25}(DMBT)_{18}]^-$ NC (m/z 5166), toward higher mass species, $[Ag_{24}Au(DMBT)_{18}]^-$ (m/z 5255) and $[Ag_{23}Au_2(DMBT)_{18}]^-$ (m/z 5344) NCs, where the former was a major and the latter was a minor product. However, a slower reaction time (∼3 h) can be attributed to a hindered interparticle approach because of the geometrically complicated interface compared to the DMBT-capped system (∼0.5 h) (further discussion in Section 3.6). Our mass spectral measurements are consistent with the time-dependent optical absorption spectra (Figure S24). In reaction@NP, the average size of Au@BDT NPs changes after reaction with $[Ag_{25}(DMBT)_{18}]^-$ NC from 3.70 ± 0.48 nm (Figure S25A) to 3.17 ± 0.42 nm (Figure S25B), and the fwhm values are 1.08 and 0.95 nm, respectively. However, unlike the DMBT-capped-interparticle system, we did not observe much change in the overall particle size distribution. The optical absorption spectrum of Au@BDT NPs showed a blue-shifted and enhanced SPR on reaction with $[Ag_{25}(DMBT)_{18}]^-$ NC, indicating a Ag-doping in Au@BDT NPs (Figure S26). Therefore, the Au@BDT NP−$[Ag_{25}(DMBT)_{18}]^-$ NC reaction proceeds via a metal-only exchange, as supported by the data from both the reaction@NP and the reaction@NC.

Next, while maintaining the complexity of the reacting interface (Au-DMBT···Ag-BDT), we studied the particle system with reversed monolayer coverage, such as Au@DMBT NP and $[Ag_{29}(BDT)_{12}(TPP)_4]^{3-}$ NC. The reaction@NP and reaction@NC for the particle system were performed along a similar line as in the previous one. As for the reaction@NP, TEM images (Figure S27) and optical spectral data (Figure S28) suggested that individual particles in the NP−NC mixture remained unreacted in solution for the entire period of measurement. In the time-dependent ESI MS study for the reaction@NC, the $[Ag_{29}(BDT)_{12}]^{3-}$ NC peak (m/z 1603) remained intact in the solution even after 24 h, also suggesting

https://doi.org/10.1021/acs.chemmater.4c00620
Chem. Mater. XXXX, XXX, XXX−XXX

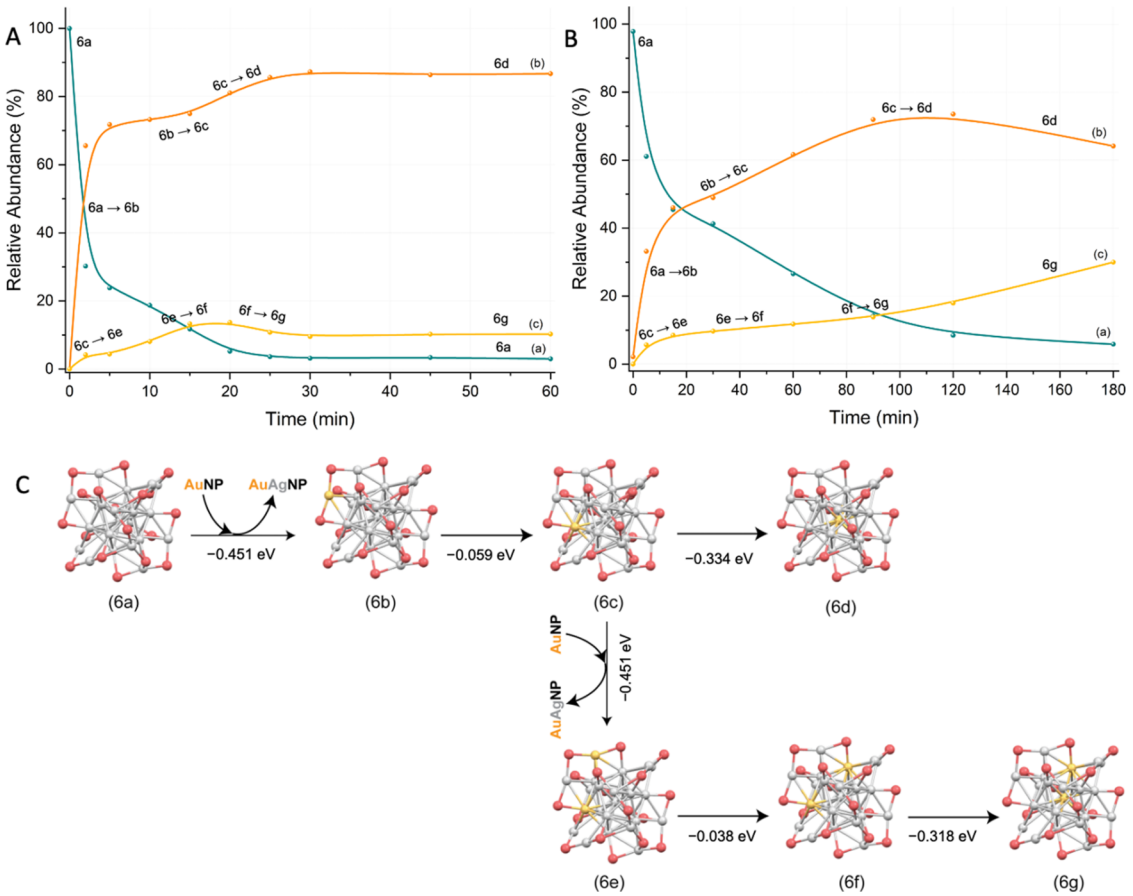

Figure 6. Plot showing the extent of the relative metal exchange (%) as a function of reaction time (in min) for the $[Ag_{25}(DMBT)_{18}]^-$ NC with Au@DMBT (A) and Au@BDT NP (B) interparticle systems. (C) Proposed mechanism of Au-doping in parent $[Ag_{25}(DMBT)_{18}]^-$ NC (a) and the corresponding reaction energies resulting in $[Ag_{24}Au(DMBT)_{18}]^-$ (b) and $[Ag_{23}Au_2(DMBT)_{18}]^-$ NCs (c). Color code: yellow, Au; gray, Ag; pink, S. C and H are omitted for simplification.

no reaction with the NP (Figure S29). The corresponding optical spectra agree with the mass spectral observations (Figure S30).

Using Au-BDT···Ag-FTP as a model, we further investigated the absence of ligand participation in NP−NC reactions with a geometrically complex interparticle interface, similar to those observed between Au-BDT···Ag-DMBT. We chose Au@BDT NP and $[PPh_4]_n[Ag_{44}(FTP)_{30}]$ NC as our particle systems where Au-BDT···Ag-FTP acts as a reacting interface (reaction@NC and reaction@NP results are provided in SI, Figure S31). The Au@BDT NP and $[Ag_{44}(FTP)_{30}]^{3-}$ NC reaction proceeds via an interparticle metal-only exchange pathway, as schematically represented in Figure S31A. In ESI MS measurement as shown in Figure S31B, within 5 min of reaction, we observed a rapid shift in the molecular peak corresponding to the parent species, $[Ag_{44}(FTP)_{30}]^{3-}$ NC (m/z 2851), toward lower and higher mass species, $[Ag_{43}(FTP)_{30}]^{3-}$ (m/z 2816) and $[Ag_{43}Au(FTP)_{30}]^{3-}$ (m/z 2881) NCs, respectively, where the former was a minor product and later was major (isotopic distributions are matched in Figure S31C). No significant mass spectral signals were detected in the MS region associated with $[Ag_{44}(FTP)_{30}]^{4-}$ NC (m/z 2070−2220) during the reaction. Based on the mass spectral intensity, we presume that $[Ag_{44}(FTP)_{30}]^{3-}$ and $[Ag_{44}(FTP)_{30}]^{4-}$ NCs upon reaction with Au@BDT NP undergo a Ag loss to form transient $[Ag_{43}(FTP)_{30}]^{3-}$ NC followed by a Ag−Au exchange to form a stable $[Ag_{43}Au(FTP)_{30}]^{3-}$ intermediate species. However, determining an accurate interparticle reaction pathway requires additional investigations. Noticeable deviations from the parent $[Ag_{44}(FTP)_{30}]^{3-}$ NC features were observed in the optical spectrum acquired within 5 min of mixing the particles, and the spectrum resembled Au-doped-Ag_{44}@FTP NC (Figure S31D).[95] In the case of reaction@NP, the optical absorption spectrum exhibited a gradual blue shift in SPR of Au@BDT NPs with time, upon reaction with $[Ag_{44}(FTP)_{30}]^{3-}$ NC, indicating Ag-diffusion in the parent Au NP (Figure S31E and schematically illustrated in Figure S31F). The parent Au@BDT NPs were monodispersed in nature and exhibited no assembling tendency (TEM image in Figure S31G-a). Interestingly, the reacted NPs self-assembled in the solution to create sphere-like superstructures; a similar phenomenon was previously reported with Ag- and Cu-doped Au particles (Figure S31H-a).[71,74] Upon reaction with $[Ag_{44}(FTP)_{30}]^{3-}$ NC, the average size of Au@BDT NPs changed from 3.70 ± 0.48 nm (Figure S31G-b) to 3.01 ± 0.66 nm (Figure S31H-b), and the fwhm values were 1.08 and 1.56 nm, respectively. Unlike the DMBT-capped-interparticle system, the shift in particle size distribution toward a higher fwhm value suggests that the reaction introduced a polydispersity into the Au NPs. From the above discussion, we conclude that the Au@BDT NP−$[Ag_{44}(FTP)_{30}]^{3-}$ NC reaction also proceeds via a metal-only exchange pathway.

https://doi.org/10.1021/acs.chemmater.4c00620
Chem. Mater. XXXX, XXX, XXX−XXX

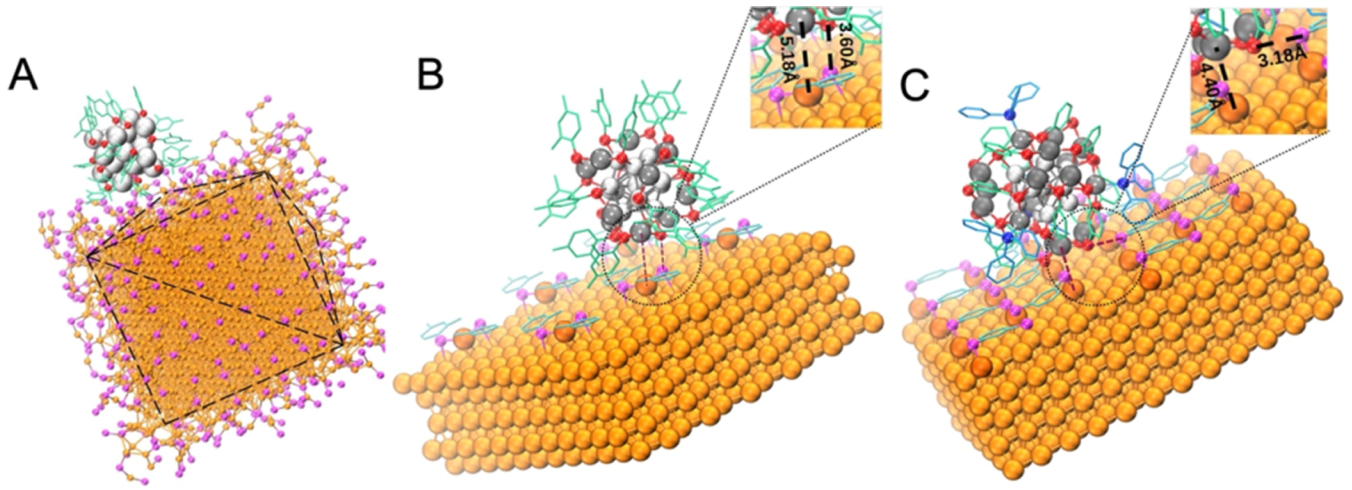

Figure 7. Docking structures of the interactions of (A) $[Ag_{25}(DMBT)_{18}]^-$ NC on SR-protected Au NP, (B) $[Ag_{25}(DMBT)_{18}]^-$ NC on DMBT-monolayered Au(111) surface, and (C) $[Ag_{29}(BDT)_{12}(TPP)_4]^{3-}$ NC on BDT-monolayered Au(111) surface. Color code: gold, Au; orange, Au_{ad}; gray, Ag NC staple; silver, Ag NC icosahedron; magenta, S of surface ligands; red, S of NC ligands; cyan, C of surface ligands; light green, C of thiolate NC ligands, sky blue, C of TPP ligands; blue, P. H was omitted for clarity.

3.5. Relative Abundance Plots. To better understand the kinetics of atom exchange in an interparticle reaction, we investigated the trend in the abundance (%) of reactant and product NCs as a function of reaction time (Figure 6). In this context, the relative abundance (%) refers to the intensity of an ion of a parent or a product relative to the total parent and product ions at a given time. We assumed that the abundance of the parent NC was 100% at a zero reaction time.

As discussed in the previous section, the Au@DMBT NP and $[Ag_{25}(DMBT)_{18}]^-$ NC reactions proceed via alloy−NC intermediates where $[Ag_{24}Au(DMBT)_{18}]^-$ and $[Ag_{23}Au_2(DMBT)_{18}]^-$ NCs were identified as major and minor products, respectively (Figure 3B). Initially, we observed a rapid conversion of the parent $[Ag_{25}(DMBT)_{18}]^-$ NC into its first-doped $[Ag_{24}Au(DMBT)_{18}]^-$ product, while the second-doped $[Ag_{23}Au_2(DMBT)_{18}]^-$ product appeared at a much slower rate (Figure 6A). The $[Ag_{25}(DMBT)_{18}]^-$ and $[Ag_{24}Au(DMBT)_{18}]^-$ NCs have an analogous crystal structure with an M_{13} icosahedron core and six $M_2(SR)_3$ motifs, where M and SR refer to metal and thiolate, respectively. It is reported that doping in $[Ag_{25}(DMBT)_{18}]^-$ to $[Ag_{24}Au(DMBT)_{18}]^-$ NCs occurs in a nanogymnastic fashion, with metal exchange beginning at the staple and progressing to the Au_{13} icosahedron core.[99] The reaction energy (ΔE) values for each step were computed using density functional theory (DFT); further discussion in Section 3.6. The possible explanation for faster 6a → 6b (ΔE = −0.45152 eV) conversion of the $[Ag_{25}(DMBT)_{18}]^-$ (6a) to highly stable $[Ag_{24}Au(DMBT)_{18}]^-$ (6b) might be attributed to an interparticle Au−Ag exchange of the surface atoms (Figure 6C). Next, the intrananocluster atomic exchange involves rapid swapping at the staple (6b → 6c, ΔE = −0.05984 eV) followed by a slower diffusion into the core (6c → 6d, ΔE = −0.33456 eV) until equilibrium is attained. The interaction between Au@DMBT NP and $[Ag_{24}Au(DMBT)_{18}]^-$ NC results in the infusion of a second Au-atom, which presumably accounts for the slowest rate of conversion to $[Ag_{23}Au_2(DMBT)_{18}]^-$ (6g). As per our calculations, the second Au-atom replaces a Ag-atom at the staple position in $Ag_{24}Au_{Ih}$ (6c → 6e, ΔE = −0.45152 eV) followed by intrananocluster swapping rearrangements (6e → 6f, ΔE = −0.03808 eV and 6f → 6g, ΔE = −0.31824 eV). We believe that the overall interparticle reaction kinematics would be much more complex if the byproducts were also considered.

Similarly, the reaction of Au@BDT NP and $[Ag_{25}(DMBT)_{18}]^-$ NC involves an intersystem metal-only hopping where the $[Ag_{24}Au(DMBT)_{18}]^-$ and $[Ag_{23}Au_2(DMBT)_{18}]^-$ NCs were identified as the major and minor products, respectively (Figure 5D). Herein, the $[Ag_{25}(DMBT)_{18}]^-$ to $[Ag_{24}Au(DMBT)_{18}]^-$ conversion is much slower than the previous one (Figure 6B). The longer reaction time scale may be due to the sterically hindered interparticle interaction at the metal−ligand interface before metal exchange. The mechanism of Au-hopping during the doping reaction presumably takes a similar path, as explained in Figure 6C. We infer that the interparticle reaction time scale depends on the metal−ligand bond and the rigidity of the reaction interface.

3.6. Computational Studies. To understand the driving force and mechanism behind the interparticle reactions, we used the density functional theory (DFT) combined with molecular docking (computational details in SI3). Molecular dynamics (MD) simulation of octahedral-shaped Au@SR NPs suggests a surface coverage of Au-SR staples and longer Au-SR chains.[100] Staple and ligand coverage on the facets is heterogeneous, lowest at the vertices where the four faces meet and at the edges between neighboring facets.[100] Lower coverage areas on the NP surface may be sterically more accessible for a facile reaction.

The Ag NC docking on the octahedron Au NP suggests that the Ag NC approaches one of the octahedral facets of the NP and interacts with Au−S staples and chains, ligands, and the bare gold surface of the NP (Figure 7A). To simplify the calculations, we assumed a Au(111) surface with a variable monolayer coverage instead of an octahedral Au NP to interact with Ag NC (detailed discussion on the surface construction in the SI4 and Figures S32−S33). Docking interactions of the $[Ag_{25}(DMBT)_{18}]^-$ and $[Ag_{29}(BDT)_{12}(TPP)_4]^{3-}$ NCs are with 2,4-DMBT (Figure 7B) and 1,3-BDT (Figure 7C)-monolayered Au(111) surfaces at a low ligand and staple coverage, respectively (interatomic distances are highlighted in the inset). A comprehensive analysis of the Ag NC−Au(111)@SR

https://doi.org/10.1021/acs.chemmater.4c00620
Chem. Mater. XXXX, XXX, XXX−XXX

surface docking interaction at different extents of monolayer coverage in terms of binding energies (BEs) is presented in SI 5 and 6 (Figures S34–S36 and Tables S1 and S2).

We calculated reaction energetics to understand the thermodynamic feasibility of the interparticle reactions. Based on our DFT calculations, the most favorable Au-doping route in $[Ag_{25}(DMBT)_{18}]^-$ NC is via the $Ag_2(DMBT)_3$ staple, the Ag_{13} icosahedron, and finally, the icosahedron core (refer to Figure 6C in Section 3.5 and energy values in Tables S3 and S4). In $[Ag_{23}Au_2(DMBT)_{18}]^-$ NC, the second Ag-atom preferably occupies the Au_{13} icosahedron position (Figure 6C and energy values in Table S5). Similarly, $[Ag_{28}Au(BDT)_{12}(TPP)_4]^{3-}$ NC has its most favorable geometry with Au in the core position (refer to Figure S37 and energy values in Table S6).

Next, we used a 2 × 1 supercell of the Au(111) surface derived from a (3 × 4) unit cell to calculate the metallic exchange reaction energies (ΔE) between the Ag NCs and Au(111)@SR surface models (surface description in computation details, SI). Our simulations show that upon reaction, Ag-atom preferably occupies the inner layers of the Au(111) surface instead of the staple or top layer (Figure S38 and ΔE values in Tables S7–S9). Figure S39 shows a comparison of the reaction energies for the NC–surface reactions: (1) $[Ag_{25}(DMBT)_{18}]^-$–Au(111)@DMBT (ΔE = 0.0019 Ha), (2) $[Ag_{29}(BDT)_{12}(TPP)_4]^{3-}$–Au(111)@BDT ($\Delta E$ = 0.0128 Ha), (3) $[Ag_{25}(DMBT)_{18}]^-$–Au(111)@BDT (ΔE = 0.0038 Ha), and (4) $[Ag_{29}(BDT)_{12}(TPP)_4]^{3-}$–Au(111)@DMBT ($\Delta E$ = 0.0109 Ha). Reactions (1) and (3) are more feasible than (2) and (4) based on the ΔE values, consistent with our experimental results. However, the calculations suggest that the reactions are slightly endothermic as the optimizations were performed under conditions equivalent to zero temperature. At room temperature, the entropic term ($-T\Delta S$) is expected to further lower the Gibbs free energy so that ΔG becomes negative. This leads to a spontaneous reaction, as observed in our experiments with $[Ag_{25}(DMBT)_{18}]^-$ NC. Further, the small positive reaction energies for reactions with $[Ag_{25}(DMBT)_{18}]^-$ NC (reactions 1 and 3) compared to that with $[Ag_{29}(BDT)_{12}(TPP)_4]^{3-}$ NC (reactions 2 and 4) indicate a low reaction barrier for the former. Therefore, $[Ag_{25}(DMBT)_{18}]^-$ NC is more reactive toward the Au(111)@SR surface, which is true regardless of the presence of DMBT or BDT monolayers and is consistent with our experimental observations.

Overall, we have found that the $[Ag_{25}(DMBT)_{18}]^-$ NC binds more strongly to Au(111) monolayer surfaces for low coverages, which are expected to favor the reaction as the surface Au and staple Au and S atoms are sterically more accessible, and that the Ag/Au atomic exchange between the Ag NC and the Au(111)@DMBT is slightly more favorable for $[Ag_{25}(DMBT)_{18}]^-$ as the reaction energies are smaller. The steric hindrance effects of the slightly larger $[Ag_{29}(BDT)_{12}(TPP)_4]^{3-}$ NC with bulky TPP groups are likely to be greater, leading to higher energy barriers for the reaction of $[Ag_{29}(BDT)_{12}(TPP)_4]^{3-}$ compared to $[Ag_{25}(DMBT)_{18}]^-$, and hence the reaction does not occur. Mechanistically, the calculated reaction energies between different symmetry sites of the NC and surface indicate that the substitution of Ag-atoms into the deeper layers is more feasible, while Au-atoms prefer to occupy the central-atom position and icosahedral sites of the Ag NC.

4. CONCLUSIONS

In summary, we demonstrated AGRs in plasmonic Au NPs with atomically precise Ag NCs where the interparticle metal–ligand interface controls the overall reaction dynamics. Au@DMBT NPs on reaction with $[Ag_{25}(DMBT)_{18}]^-$ NC resulted in well-alloyed bimetallic NPs. Reaction-driven transformations in the morphology and composition of the Au NPs were studied using HAADF-STEM equipped with EDS. With the introduction of dithiol-induced geometric rigidity at the interface, no reaction was observed for the Au@BDT NP··· $[Ag_{29}(BDT)_{12}(TPP)_4]^{3-}$ NC systems. ESI MS studies confirmed that the reactions involve interparticle metal–ligand and metal-only exchanges in the case of monothiol- and dithiol-capped NPs, respectively. DFT calculation also confirmed that the overall metal-exchange reactions energetically favor the DMBT-capped particle system over the BDT-capped system. Further electrochemical, *in situ* microscopic, and molecular dynamics studies are required to fully comprehend the phenomena behind such reactions. The universality of NP–NC reactions throughout the noble metal system can be further extended to prepare multimetallic alloy particles with controlled size and composition.

■ ASSOCIATED CONTENT

Supporting Information

The Supporting Information is available free of charge at https://pubs.acs.org/doi/10.1021/acs.chemmater.4c00620.

Materials and methods, concentration calculations, UV–vis, ESI MS, TEM, EDS, Raman characterization of particles, and detailed computational analysis of the interparticle reactions (PDF)

■ AUTHOR INFORMATION

Corresponding Authors

Sharma S. R. K. C. Yamijala − *Department of Chemistry, Indian Institute of Technology Madras, Chennai 600036, India;* orcid.org/0000-0003-1773-9226; Email: yamijala@iitm.ac.in

Nonappa − *Faculty of Engineering and Natural Sciences, Tampere University, FI-33720 Tampere, Finland;* orcid.org/0000-0002-6804-4128; Email: nonappa@tuni.fi

Thalappil Pradeep − *DST Unit of Nanoscience (DST UNS) and Thematic Unit of Excellence (TUE), Department of Chemistry, Indian Institute of Technology Madras, Chennai 600036, India; International Centre for Clean Water, Chennai 600113, India;* orcid.org/0000-0003-3174-534X; Email: pradeep@iitm.ac.in

Authors

Paulami Bose − *DST Unit of Nanoscience (DST UNS) and Thematic Unit of Excellence (TUE), Department of Chemistry, Indian Institute of Technology Madras, Chennai 600036, India;* Present Address: Faculty of Engineering and Natural Sciences, Tampere University, FI-33720 Tampere, Finland

Jayoti Roy − *DST Unit of Nanoscience (DST UNS) and Thematic Unit of Excellence (TUE), Department of Chemistry, Indian Institute of Technology Madras, Chennai 600036, India*

Vikash Khokhar − *DST Unit of Nanoscience (DST UNS) and Thematic Unit of Excellence (TUE), Department of*

https://doi.org/10.1021/acs.chemmater.4c00620
Chem. Mater. XXXX, XXX, XXX−XXX

Chemistry, Indian Institute of Technology Madras, Chennai 600036, India

Biswajit Mondal − *DST Unit of Nanoscience (DST UNS) and Thematic Unit of Excellence (TUE), Department of Chemistry, Indian Institute of Technology Madras, Chennai 600036, India*

Ganapati Natarajan − *International Centre for Clean Water, Chennai 600113, India*

Sujan Manna − *DST Unit of Nanoscience (DST UNS) and Thematic Unit of Excellence (TUE), Department of Chemistry, Indian Institute of Technology Madras, Chennai 600036, India*

Vivek Yadav − *DST Unit of Nanoscience (DST UNS) and Thematic Unit of Excellence (TUE), Department of Chemistry, Indian Institute of Technology Madras, Chennai 600036, India*

Anupriya Nyayban − *DST Unit of Nanoscience (DST UNS) and Thematic Unit of Excellence (TUE), Department of Chemistry, Indian Institute of Technology Madras, Chennai 600036, India*

Complete contact information is available at: https://pubs.acs.org/10.1021/acs.chemmater.4c00620

Author Contributions

P.B. performed the experiments and analyzed the results. J.R. carried out the MS measurements. B.M. and N.N. carried out the EM imaging. V.K., G.N., A.N., and S.S.R.K.C.Y. carried out the calculations. S.M. carried out the Raman measurements. P.B. and V.Y. performed the syntheses. T.P. was the project designer and supervisor, overseeing the progress. Every author made a contribution to the writing of the manuscript.

Notes

The authors declare no competing financial interest.

■ ACKNOWLEDGMENTS

The authors acknowledge the Department of Science and Technology (DST), Government of India, and the Centre of Excellence program of the Indian Institute of Technology Madras, on the theme of Molecular Materials and Functions, under the Institutions of Eminence of Ministry of Education, India, for supporting their research. The authors also thank the Academy of Finland for project funding (No. 352900), the Photonics Research and Innovation (PREIN) flagship, and the Tampere Microscopy Centre for imaging facilities. The authors are grateful to Anirban Som, Indian Institute of Technology Madras, for his insightful comments that helped to shape the manuscript in its final form. The authors also thank Bhanupriya S. for her technical assistance with the electron microscopic facility at the DST Unit of Nanoscience, Indian Institute of Technology Madras. T.P. thanks the Science and Engineering Research Board (SERB), India, for funding through the SPR/2021/000439 research grant and a JC Bose Fellowship.

■ DEDICATION

Dedicated to Prof. C. N. R. Rao on the occasion of his 90th birthday.

■ REFERENCES

(1) Haldar, K. K.; Kundu, S.; Patra, A. Core-Size-Dependent Catalytic Properties of Bimetallic Au/Ag Core−Shell Nanoparticles. *ACS Appl. Mater. Interfaces* **2014**, *6* (24), 21946−21953.

(2) Gellé, A.; Jin, T.; de la Garza, L.; Price, G. D.; Besteiro, L. V.; Moores, A. Applications of Plasmon-Enhanced Nanocatalysis to Organic Transformations. *Chem. Rev.* **2020**, *120* (2), 986−1041.

(3) Rebello Sousa Dias, M.; Leite, M. S. Alloying: A Platform for Metallic Materials with On-Demand Optical Response. *Acc. Chem. Res.* **2019**, *52* (10), 2881−2891.

(4) Vasicek, T. W.; Kress, P. M.; Jenkins, S. V. Optical Properties of Alloyed Noble Metal Nanoparticles: A Nanotechnology Experiment for Chemistry and Engineering Students. *J. Chem. Educ.* **2020**, *97* (10), 3778−3783.

(5) Gilroy, K. D.; Ruditskiy, A.; Peng, H. C.; Qin, D.; Xia, Y. Bimetallic Nanocrystals: Syntheses, Properties, and Applications. *Chem. Rev.* **2016**, *116* (18), 10414−10472.

(6) Xia, X.; Wang, Y.; Ruditskiy, A.; Xia, Y. 25th Anniversary Article: Galvanic Replacement: A Simple and Versatile Route to Hollow Nanostructures with Tunable and Well-Controlled Properties. *Adv. Mater.* **2013**, *25* (44), 6313−6333.

(7) da Silva, A. G. M.; Rodrigues, T. S.; Haigh, S. J.; Camargo, P. H. C. Galvanic Replacement Reaction: Recent Developments for Engineering Metal Nanostructures towards Catalytic Applications. *Chem. Commun.* **2017**, *53* (53), 7135−7148.

(8) Ha, M.; Kim, J. H.; You, M.; Li, Q.; Fan, C.; Nam, J. M. Multicomponent Plasmonic Nanoparticles: From Heterostructured Nanoparticles to Colloidal Composite Nanostructures. *Chem. Rev.* **2019**, *119* (24), 12208−12278.

(9) Cheng, H.; Wang, C.; Qin, D.; Xia, Y. Galvanic Replacement Synthesis of Metal Nanostructures: Bridging the Gap between Chemical and Electrochemical Approaches. *Acc. Chem. Res.* **2023**, *56* (7), 900−909.

(10) Gan, Z.; Xia, N.; Wu, Z. Discovery, Mechanism, and Application of Antigalvanic Reaction. *Acc. Chem. Res.* **2018**, *51* (11), 2774−2783.

(11) Zhu, M.; Wang, P.; Yan, N.; Chai, X.; He, L.; Zhao, Y.; Xia, N.; Yao, C.; Li, J.; Deng, H.; Zhu, Y.; Pei, Y.; Wu, Z. The Fourth Alloying Mode by Way of Anti-Galvanic Reaction. *Angew. Chem., Int. Ed.* **2018**, *57* (17), 4500−4504.

(12) Murray, R. W. Nanoelectrochemistry: Metal Nanoparticles, Nanoelectrodes, and Nanopores. *Chem. Rev.* **2008**, *108* (7), 2688−2720.

(13) Jin, R.; Zeng, C.; Zhou, M.; Chen, Y. Atomically Precise Colloidal Metal Nanoclusters and Nanoparticles: Fundamentals and Opportunities. *Chem. Rev.* **2016**, *116* (18), 10346−10413.

(14) Chakraborty, I.; Pradeep, T. Atomically Precise Clusters of Noble Metals: Emerging Link between Atoms and Nanoparticles. *Chem. Rev.* **2017**, *117* (12), 8208−8271.

(15) Ghosh, A.; Mohammed, O. F.; Bakr, O. M. Atomic-Level Doping of Metal Clusters. *Acc. Chem. Res.* **2018**, *51* (12), 3094−3103.

(16) Kang, X.; Zhu, M. Tailoring the Photoluminescence of Atomically Precise Nanoclusters. *Chem. Soc. Rev.* **2019**, *48* (8), 2422−2457.

(17) Du, Y.; Sheng, H.; Astruc, D.; Zhu, M. Atomically Precise Noble Metal Nanoclusters as Efficient Catalysts: A Bridge between Structure and Properties. *Chem. Rev.* **2020**, *120* (2), 526−622.

(18) Plieth, W. J. The Work Function of Small Metal Particles and Its Relation to Electrochemical Properties. *Surf. Sci.* **1985**, *156*, 530−535.

(19) Bonanni, A.; Pumera, M.; Miyahara, Y. Influence of Gold Nanoparticle Size (2−50 Nm) upon Its Electrochemical Behavior: An Electrochemical Impedance Spectroscopic and Voltammetric Study. *Phys. Chem. Chem. Phys.* **2011**, *13* (11), 4980−4986.

(20) Masitas, R. A.; Zamborini, F. P. Oxidation of Highly Unstable < 4 Nm Diameter Gold Nanoparticles 850 mV Negative of the Bulk Oxidation Potential. *J. Am. Chem. Soc.* **2012**, *134* (11), 5014−5017.

(21) Brainina, Kh. Z.; Galperin, L. G.; Vikulova, EV.; Stozhko, N. Yu.; Murzakaev, AM.; Timoshenkova, OR.; Kotov, YA. Gold Nanoparticles Electrooxidation: Comparison of Theory and Experiment. *J. Solid State Electrochem.* **2011**, *15* (5), 1049−1056.

(22) Pattadar, D. K.; Zamborini, F. P. Size Stability Study of Catalytically Active Sub-2 Nm Diameter Gold Nanoparticles

Synthesized with Weak Stabilizers. *J. Am. Chem. Soc.* **2018**, *140* (43), 14126−14133.
(23) Pattadar, D. K.; Masitas, R. A.; Stachurski, C. D.; Cliffel, D. E.; Zamborini, F. P. Reversing the Thermodynamics of Galvanic Replacement Reactions by Decreasing the Size of Gold Nanoparticles. *J. Am. Chem. Soc.* **2020**, *142* (45), 19268−19277.
(24) Wu, Z.; Wang, M.; Yang, J.; Zheng, X.; Cai, W.; Meng, G.; Qian, H.; Wang, H.; Jin, R. Well-Defined Nanoclusters as Fluorescent Nanosensors: A Case Study on Au25(SG)18. *Small* **2012**, *8* (13), 2028−2035.
(25) Choi, J.-P.; Fields-Zinna, C. A.; Stiles, R. L.; Balasubramanian, R.; Douglas, A. D.; Crowe, M. C.; Murray, R. W. Reactivity of [Au25(SCH2CH2Ph)18]1− Nanoparticles with Metal Ions. *J. Phys. Chem. C* **2010**, *114* (38), 15890−15896.
(26) Wu, Z. Anti-Galvanic Reduction of Thiolate-Protected Gold and Silver Nanoparticles. *Angew. Chem., Int. Ed.* **2012**, *51* (12), 2934−2938.
(27) Tian, S.; Yao, C.; Liao, L.; Xia, N.; Wu, Z. Ion-Precursor and Ion-Dose Dependent Anti-Galvanic Reduction. *Chem. Commun.* **2015**, *51* (59), 11773−11776.
(28) Wang, M.; Wu, Z.; Chu, Z.; Yang, J.; Yao, C. Chemico-Physical Synthesis of Surfactant- and Ligand-Free Gold Nanoparticles and Their Anti-Galvanic Reduction Property. *Chem. - Asian J.* **2014**, *9* (4), 1006−1010.
(29) Sun, J.; Wu, H.; Jin, Y. Synthesis of Thiolated Ag/Au Bimetallic Nanoclusters Exhibiting an Anti-Galvanic Reduction Mechanism and Composition-Dependent Fluorescence. *Nanoscale* **2014**, *6* (10), 5449−5457.
(30) Sahu, P.; Prasad, B. L. V. Preparation of Ag(Shell)−Au(Core) Nanoparticles by Anti-Galvanic Reactions: Are Capping Agents the "Real Heroes" of Reduction? *Colloids Surf., A* **2015**, *478*, 30−35.
(31) Wang, S.; Abroshan, H.; Liu, C.; Luo, T.-Y.; Zhu, M.; Kim, H. J.; Rosi, N. L.; Jin, R. Shuttling Single Metal Atom into and out of a Metal Nanoparticle. *Nat. Commun.* **2017**, *8* (1), No. 848.
(32) Li, Q.; Luo, T.-Y.; Taylor, M. G.; Wang, S.; Zhu, X.; Song, Y.; Mpourmpakis, G.; Rosi, N. L.; Jin, R. Molecular "Surgery" on a 23-Gold-Atom Nanoparticle. *Sci. Adv.* **2017**, *3* (5), No. e1603193.
(33) Wang, Z.; Senanayake, R.; Aikens, C. M.; Chen, W. M.; Tung, C. H.; Sun, D. Gold-Doped Silver Nanocluster [Au3Ag38(SCH2Ph)-24 × 5]2- (X = Cl or Br). *Nanoscale* **2016**, *8* (45), 18905−18911.
(34) Yang, Y.; Jia, T.; Han, Y.-Z.; Nan, Z.-A.; Yuan, S.-F.; Yang, F.-L.; Sun, D. An All-Alkynyl Protected 74-Nuclei Silver(I)−Copper(I)-Oxo Nanocluster: Oxo-Induced Hierarchical Bimetal Aggregation and Anisotropic Surface Ligand Orientation. *Angew. Chem., Int. Ed.* **2019**, *58* (35), 12280−12285.
(35) Han, B.-L.; Wang, Z.; Gupta, R. K.; Feng, L.; Wang, S.; Kurmoo, M.; Gao, Z.-Y.; Schein, S.; Tung, C.-H.; Sun, D. Precise Implantation of an Archimedean Ag@Cu12 Cuboctahedron into a Platonic Cu4Bis(Diphenylphosphino)Hexane6 Tetrahedron. *ACS Nano* **2021**, *15* (5), 8733−8741.
(36) Pradeep, T. *Atomically Precise Metal Nanoclusters*; Elsevier, 2022.
(37) Knoppe, S.; Bürgi, T. The Fate of Au25(SR)18 Clusters upon Ligand Exchange with Binaphthyl-Dithiol: Interstaple Binding vs. Decomposition. *Phys. Chem. Chem. Phys.* **2013**, *15* (38), 15816−15820.
(38) Niihori, Y.; Kikuchi, Y.; Kato, A.; Matsuzaki, M.; Negishi, Y. Understanding Ligand-Exchange Reactions on Thiolate-Protected Gold Clusters by Probing Isomer Distributions Using Reversed-Phase High-Performance Liquid Chromatography. *ACS Nano* **2015**, *9* (9), 9347−9356.
(39) Huang, Z.; Ishida, Y.; Narita, K.; Yonezawa, T. Kinetics of Cationic-Ligand-Exchange Reactions in Au25 Nanoclusters. *J. Phys. Chem. C* **2018**, *122* (31), 18142−18150.
(40) Zeng, C.; Liu, C.; Pei, Y.; Jin, R. Thiol Ligand-Induced Transformation of Au38(SC2H4Ph)24 to Au36(SPh-t-Bu)24. *ACS Nano* **2013**, *7* (7), 6138−6145.
(41) Zeng, C.; Chen, Y.; Das, A.; Jin, R. Transformation Chemistry of Gold Nanoclusters: From One Stable Size to Another. *J. Phys. Chem. Lett.* **2015**, *6* (15), 2976−2986.
(42) Kang, X.; Zhu, M. Transformation of Atomically Precise Nanoclusters by Ligand-Exchange. *Chem. Mater.* **2019**, *31* (24), 9939−9969.
(43) Heinecke, C. L.; Ni, T. W.; Malola, S.; Mäkinen, V.; Wong, O. A.; Häkkinen, H.; Ackerson, C. J. Structural and Theoretical Basis for Ligand Exchange on Thiolate Monolayer Protected Gold Nanoclusters. *J. Am. Chem. Soc.* **2012**, *134* (32), 13316−13322.
(44) Knoppe, S.; Dharmaratne, A. C.; Schreiner, E.; Dass, A.; Bürgi, T. Ligand Exchange Reactions on Au38 and Au40 Clusters: A Combined Circular Dichroism and Mass Spectrometry Study. *J. Am. Chem. Soc.* **2010**, *132* (47), 16783−16789.
(45) Knoppe, S.; Azoulay, R.; Dass, A.; Bürgi, T. In Situ Reaction Monitoring Reveals a Diastereoselective Ligand Exchange Reaction between the Intrinsically Chiral Au38(SR)24 and Chiral Thiols. *J. Am. Chem. Soc.* **2012**, *134* (50), 20302−20305.
(46) Wang, S.; Song, Y.; Jin, S.; Liu, X.; Zhang, J.; Pei, Y.; Meng, X.; Chen, M.; Li, P.; Zhu, M. Metal Exchange Method Using Au25 Nanoclusters as Templates for Alloy Nanoclusters with Atomic Precision. *J. Am. Chem. Soc.* **2015**, *137* (12), 4018−4021.
(47) Niihori, Y.; Hossain, S.; Kumar, B.; Nair, L. V.; Kurashige, W.; Negishi, Y. Perspective: Exchange Reactions in Thiolate-Protected Metal Clusters. *Apl. Mater.* **2017**, *5*, No. 053201.
(48) Zhang, B.; Safonova, O. V.; Pollitt, S.; Salassa, G.; Sels, A.; Kazan, R.; Wang, Y.; Rupprechter, G.; Barrabés, N.; Bürgi, T. On the Mechanism of Rapid Metal Exchange between Thiolate-Protected Gold and Gold/Silver Clusters: A Time-Resolved in Situ XAFS Study. *Phys. Chem. Chem. Phys.* **2018**, *20* (7), 5312−5318.
(49) Wang, S.; Xiong, L.; Sun, G.; Tang, L.; Zhang, J.; Pei, Y.; Zhu, M. The Mechanism of Metal Exchange in Non-Metallic Nanoclusters. *Nanoscale Adv.* **2020**, *2* (2), 664−668.
(50) Chakraborty, P.; Nag, A.; Natarajan, G.; Bandyopadhyay, N.; Paramasivam, G.; Panwar, M. K.; Chakrabarti, J.; Pradeep, T. Rapid Isotopic Exchange in Nanoparticles. *Sci. Adv.* **2019**, *5* (1), No. eaau7555.
(51) Tang, L.; Kang, X.; Wang, X.; Zhang, X.; Yuan, X.; Wang, S. Dynamic Metal Exchange between a Metalloid Silver Cluster and Silver(I) Thiolate. *Inorg. Chem.* **2021**, *60* (5), 3037−3045.
(52) Chakraborty, P.; Bose, P.; Roy, J.; Nag, A.; Mondal, B.; Chakraborty, A.; Pradeep, T. Isotopic Exchange of Atomically Precise Nanoclusters with Materials of Varying Dimensions: From Nanoscale to Bulk. *J. Phys. Chem. C* **2021**, *125* (29), 16110−16117.
(53) Yao, Q.; Wu, Z.; Liu, Z.; Lin, Y.; Yuan, X.; Xie, J. Molecular Reactivity of Thiolate-Protected Noble Metal Nanoclusters: Synthesis, Self-Assembly, and Applications. *Chem. Sci.* **2021**, *12* (1), 99−127.
(54) Bose, P.; Ramankutty, K. K.; Chakraborty, P.; Khatun, E.; Pradeep, T. A Concise Guide to Chemical Reactions of Atomically Precise Noble Metal Nanoclusters. *Nanoscale* **2024**, *16* (4), 1446−1470.
(55) Krishnadas, K. R.; Ghosh, A.; Baksi, A.; Chakraborty, I.; Natarajan, G.; Pradeep, T. Intercluster Reactions between Au25(SR)-18 and Ag44(SR)30. *J. Am. Chem. Soc.* **2016**, *138* (1), 140−148.
(56) Krishnadas, K. R.; Baksi, A.; Ghosh, A.; Natarajan, G.; Pradeep, T. Structure-Conserving Spontaneous Transformations between Nanoparticles. *Nat. Commun.* **2016**, *7* (1), No. 13447.
(57) Krishnadas, K. R.; Baksi, A.; Ghosh, A.; Natarajan, G.; Som, A.; Pradeep, T. Interparticle Reactions: An Emerging Direction in Nanomaterials Chemistry. *Acc. Chem. Res.* **2017**, *50* (8), 1988−1996.
(58) Khatun, E.; Chakraborty, P.; Jacob, B. R.; Paramasivam, G.; Bodiuzzaman, M.; Dar, W. A.; Pradeep, T. Intercluster Reactions Resulting in Silver-Rich Trimetallic Nanoclusters. *Chem. Mater.* **2020**, *32* (1), 611−619.
(59) Salassa, G.; Sels, A.; Mancin, F.; Bürgi, T. Dynamic Nature of Thiolate Monolayer in Au25(SR)18 Nanoclusters. *ACS Nano* **2017**, *11* (12), 12609−12614.

https://doi.org/10.1021/acs.chemmater.4c00620
Chem. Mater. XXXX, XXX, XXX−XXX

(60) Bürgi, T. Properties of the Gold-Sulphur Interface: From Self-Assembled Monolayers to Clusters. *Nanoscale* **2015**, *7* (38), 15553−15567.
(61) Krishnadas, K. R.; Natarajan, G.; Baksi, A.; Ghosh, A.; Khatun, E.; Pradeep, T. Metal−Ligand Interface in the Chemical Reactions of Ligand-Protected Noble Metal Clusters. *Langmuir* **2019**, *35* (35), 11243−11254.
(62) Som, A.; Samal, A. K.; Udayabhaskararao, T.; Bootharaju, M. S.; Pradeep, T. Manifestation of the Difference in Reactivity of Silver Clusters in Contrast to Its Ions and Nanoparticles: The Growth of Metal Tipped Te Nanowires. *Chem. Mater.* **2014**, *26* (10), 3049−3056.
(63) Nonappa; Lahtinen, T.; Haataja, J. S.; Tero, T.-R.; Häkkinen, H.; Ikkala, O. Template-Free Supracolloidal Self-Assembly of Atomically Precise Gold Nanoclusters: From 2D Colloidal Crystals to Spherical Capsids. *Angew. Chem., Int. Ed.* **2016**, *55* (52), 16035−16038.
(64) Som, A.; Chakraborty, I.; Maark, T. A.; Bhat, S.; Pradeep, T. Cluster-Mediated Crossed Bilayer Precision Assemblies of 1D Nanowires. *Adv. Mater.* **2016**, *28* (14), 2827−2833.
(65) Chakraborty, A.; Fernandez, A. C.; Som, A.; Mondal, B.; Natarajan, G.; Paramasivam, G.; Lahtinen, T.; Häkkinen, H.; Nonappa; Pradeep, T. Atomically Precise Nanocluster Assemblies Encapsulating Plasmonic Gold Nanorods. *Angew. Chem., Int. Ed.* **2018**, *57* (22), 6522−6526.
(66) Chakraborty, P.; Nag, A.; Chakraborty, A.; Pradeep, T. Approaching Materials with Atomic Precision Using Supramolecular Cluster Assemblies. *Acc. Chem. Res.* **2019**, *52* (1), 2−11.
(67) Chakraborty, A.; Dave, H.; Mondal, B.; Nonappa; Khatun, E.; Pradeep, T. Shell-Isolated Assembly of Atomically Precise Nanoclusters on Gold Nanorods for Integrated Plasmonic-Luminescent Nanocomposites. *J. Phys. Chem. B* **2022**, *126* (8), 1842−1851.
(68) Som, A.; Griffo, A.; Chakraborty, I.; Hähl, H.; Mondal, B.; Chakraborty, A.; Jacobs, K.; Laaksonen, P.; Ikkala, O.; Pradeep, T.; Nonappa. Strong and Elastic Membranes via Hydrogen Bonding Directed Self-Assembly of Atomically Precise Nanoclusters. *Small* **2022**, *18* (34), No. 2201707.
(69) Nonappa; Ikkala, O. Hydrogen Bonding Directed Colloidal Self-Assembly of Nanoparticles into 2D Crystals, Capsids, and Supracolloidal Assemblies. *Adv. Funct. Mater.* **2018**, *28* (27), No. 1704328.
(70) Nonappa. Precision Nanoengineering for Functional Self-Assemblies across Length Scales. *Chem. Commun.* **2023**, *59*, 13800−13819, DOI: 10.1039/D3CC02205F.
(71) Bose, P.; Chakraborty, P.; Mohanty, J. S.; Nonappa; Ray Chowdhuri, A.; Khatun, E.; Ahuja, T.; Mahendranath, A.; Pradeep, T. Atom Transfer between Precision Nanoclusters and Polydispersed Nanoparticles: A Facile Route for Monodisperse Alloy Nanoparticles and Their Superstructures. *Nanoscale* **2020**, *12* (43), 22116−22128.
(72) Kazan, R.; Muller, U.; Burgi, T. Doping of Thiolate Protected Gold Clusters through Reaction with Metal Surfaces. *Nanoscale* **2019**, *11* (6), 2938−2945.
(73) Chakraborty, A.; Stanley, M. M.; Mondal, B.; Nonappa; Bodiuzzaman, M.; Chakraborty, P.; Kannan, M. P.; Pradeep, T. Tunable Reactivity of Silver Nanoclusters: A Facile Route to Synthesize a Range of Bimetallic Nanostructures. *Nanoscale* **2023**, *15* (6), 2690−2699.
(74) Roy, J.; Mondal, B.; Vishwakarma, G.; Nonappa; Sridharan, N. V.; Krishnamurthi, P.; Pradeep, T. Dissociative Reactions of [Au25(SR)18]− at Copper Oxide Nanoparticles and Formation of Aggregated Nanostructures. *Nanoscale* **2023**, *15* (18), 8225−8234.
(75) Hou, K.; Han, J.; Tang, Z. Formation of Supraparticles and Their Application in Catalysis. *ACS Mater. Lett.* **2020**, *2* (1), 95−106.
(76) Talapin, D. V.; Lee, J.-S.; Kovalenko, M. V.; Shevchenko, E. V. Prospects of Colloidal Nanocrystals for Electronic and Optoelectronic Applications. *Chem. Rev.* **2010**, *110* (1), 389−458.
(77) García-Lojo, D.; Núñez-Sánchez, S.; Gómez-Graña, S.; Grzelczak, M.; Pastoriza-Santos, I.; Pérez-Juste, J.; Liz-Marzán, L. M. Plasmonic Supercrystals. *Acc. Chem. Res.* **2019**, *52* (7), 1855−1864.
(78) Chou, L. Y. T.; Zagorovsky, K.; Chan, W. C. W. DNA Assembly of Nanoparticle Superstructures for Controlled Biological Delivery and Elimination. *Nat. Nanotechnol.* **2014**, *9* (2), 148−155.
(79) Zhao, H.; Sen, S.; Udayabhaskararao, T.; Sawczyk, M.; Kučanda, K.; Manna, D.; Kundu, P. K.; Lee, J.-W.; Král, P.; Klajn, R. Reversible Trapping and Reaction Acceleration within Dynamically Self-Assembling Nanoflasks. *Nat. Nanotechnol.* **2016**, *11* (1), 82−88.
(80) Wang, Y.; Zeiri, O.; Raula, M.; Le Ouay, B.; Stellacci, F.; Weinstock, I. A. Host−Guest Chemistry with Water-Soluble Gold Nanoparticle Supraspheres. *Nat. Nanotechnol.* **2017**, *12* (2), 170−176.
(81) Pigliacelli, C.; Maiolo, D.; Nonappa; Haataja, J. S.; Amenitsch, H.; Michelet, C.; Sánchez Moreno, P.; Tirotta, I.; Metrangolo, P.; Baldelli Bombelli, F. Efficient Encapsulation of Fluorinated Drugs in the Confined Space of Water-Dispersible Fluorous Supraparticles. *Angew. Chem., Int. Ed.* **2017**, *56* (51), 16186−16190.
(82) Matricardi, C.; Hanske, C.; Garcia-Pomar, J. L.; Langer, J.; Mihi, A.; Liz-Marzán, L. M. Gold Nanoparticle Plasmonic Superlattices as Surface-Enhanced Raman Spectroscopy Substrates. *ACS Nano* **2018**, *12* (8), 8531−8539.
(83) Cai, J.; Zhang, W.; Xu, L.; Hao, C.; Ma, W.; Sun, M.; Wu, X.; Qin, X.; Colombari, F. M.; de Moura, A. F.; Xu, J.; Silva, M. C.; Carneiro-Neto, E. B.; Gomes, W. R.; Vallée, R. A. L.; Pereira, E. C.; Liu, X.; Xu, C.; Klajn, R.; Kotov, N. A.; Kuang, H. Polarization-Sensitive Optoionic Membranes from Chiral Plasmonic Nanoparticles. *Nat. Nanotechnol.* **2022**, *17* (4), 408−416.
(84) Rao, A.; Roy, S.; Jain, V.; Pillai, P. P. Nanoparticle Self-Assembly: From Design Principles to Complex Matter to Functional Materials. *ACS Appl. Mater. Interfaces* **2023**, *15* (21), 25248−25274.
(85) Joshi, C. P.; Bootharaju, M. S.; Alhilaly, M. J.; Bakr, O. M. [Ag25(SR)18]−: The "Golden" Silver Nanoparticle. *J. Am. Chem. Soc.* **2015**, *137* (36), 11578−11581.
(86) Cortie, M. B.; McDonagh, A. M. Synthesis and Optical Properties of Hybrid and Alloy Plasmonic Nanoparticles. *Chem. Rev.* **2011**, *111* (6), 3713−3735.
(87) Tokonami, S.; Morita, N.; Takasaki, K.; Toshima, N. Novel Synthesis, Structure, and Oxidation Catalysis of Ag/Au Bimetallic Nanoparticles. *J. Phys. Chem. C* **2010**, *114* (23), 10336−10341.
(88) Mallin, M. P.; Murphy, C. J. Solution-Phase Synthesis of Sub-10 Nm Au−Ag Alloy Nanoparticles. *Nano Lett.* **2002**, *2* (11), 1235−1237.
(89) Bootharaju, M. S.; Joshi, C. P.; Parida, M. R.; Mohammed, O. F.; Bakr, O. M. Templated Atom-Precise Galvanic Synthesis and Structure Elucidation of a [Ag24Au(SR)18]− Nanocluster. *Angew. Chem., Int. Ed.* **2016**, *55* (3), 922−926.
(90) Bodiuzzaman, M.; Khatun, E.; Sugi, K. S.; Paramasivam, G.; Dar, W. A.; Antharjanam, S.; Pradeep, T. Dithiol-Induced Contraction in Ag14 Clusters and Its Manifestation in Electronic Structures. *J. Phys. Chem. C* **2020**, *124* (42), 23426−23432.
(91) Ghosh, A.; Ghosh, D.; Khatun, E.; Chakraborty, P.; Pradeep, T. Unusual Reactivity of Dithiol Protected Clusters in Comparison to Monothiol Protected Clusters: Studies Using Ag51(BDT)19(TPP)3 and Ag29(BDT)12(TPP)4. *Nanoscale* **2017**, *9* (3), 1068−1077.
(92) Brust, M.; Walker, M.; Bethell, D.; Schiffrin, D. J.; Whyman, R. Synthesis of Thiol-Derivatised Gold Nanoparticles in a Two-Phase Liquid−Liquid System. *J. Chem. Soc., Chem. Commun.* **1994**, *0* (7), 801−802.
(93) AbdulHalim, L. G.; Bootharaju, M. S.; Tang, Q.; Del Gobbo, S.; AbdulHalim, R. G.; Eddaoudi, M.; Jiang, D. E.; Bakr, O. M. Ag29(BDT)12(TPP)4: A Tetravalent Nanocluster. *J. Am. Chem. Soc.* **2015**, *137* (37), 11970−11975.
(94) Krishnadas, K. R.; Baksi, A.; Ghosh, A.; Natarajan, G.; Pradeep, T. Manifestation of Geometric and Electronic Shell Structures of Metal Clusters in Intercluster Reactions. *ACS Nano* **2017**, *11* (6), 6015−6023.
(95) Yang, H.; Wang, Y.; Huang, H.; Gell, L.; Lehtovaara, L.; Malola, S.; Häkkinen, H.; Zheng, N. All-Thiol-Stabilized Ag44 and Au12Ag32

Nanoparticles with Single-Crystal Structures. *Nat. Commun.* **2013**, *4* (1), No. 2422.
(96) Emmons, E. D.; Guicheteau, J. A.; Fountain, A. W.; Tripathi, A. Effect of Substituents on Surface Equilibria of Thiophenols and Isoquinolines on Gold Substrates Studied Using Surface-Enhanced Raman Spectroscopy. *Phys. Chem. Chem. Phys.* **2020**, *22* (28), 15953−15965.
(97) Varsányi, G.; Láng, L.; Kovner, M. A.; Lempert, K. *Assignment for Vibrational Spectra of Seven Hundred Benzene Derivatives*; Wiley: New York, 1974.
(98) Szafranski, C. A.; Tanner, W.; Laibinis, P. E.; Garrell, R. L. Surface-Enhanced Raman Spectroscopy of Halogenated Aromatic Thiols on Gold Electrodes. *Langmuir* **1998**, *14* (13), 3580−3589.
(99) Bootharaju, M. S.; Sinatra, L.; Bakr, O. M. Distinct Metal-Exchange Pathways of Doped Ag25 Nanoclusters. *Nanoscale* **2016**, *8* (39), 17333−17339.
(100) Richardi, J.; Fadigas, M. ReaxFF Molecular Dynamics Simulations of Large Gold Nanocrystals. *J. Chem. Theory Comput.* **2022**, *18* (4), 2521−2529.

https://doi.org/10.1021/acs.chemmater.4c00620
Chem. Mater. XXXX, XXX, XXX−XXX